Modelling GIC in the Southern South Island of Aotearoa New Zealand using Magnetotelluric Data

K.M. Pratscher[1], M. Ingham[1], D.H. Mac Manus[2], M. Kruglyakov[2], W. Heise[3], C.J. Rodger[2], T. Divett[1], E. Bertrand[3], M. Dalzell[4], J. Brundell[2]

[1]School of Chemical and Physical Sciences, Victoria University of Wellington, Wellington, New Zealand.

[2]Department of Physics, University of Otago, Dunedin, New Zealand.

[3]GNS Science, Lower Hutt, New Zealand.

[4]Transpower New Zealand Ltd., Wellington New Zealand

Corresponding author: Kristin Pratscher (kristin.pratscher@vuw.ac.nz)

Key Points:

- Magnetotelluric impedances from 62 sites across southern South Island of Aotearoa New Zealand have been used to model GIC during 2 storms.
- Calculated GIC are compared to observed values at 4 transformers and GIC during sudden storm commencements are captured by MT-based models.
- Quantitative comparison between simulations confirms that consideration of spatial variations in the magnetic field is important.

Abstract

Magnetotelluric (MT) impedances from 62 sites in southern South Island of Aotearoa New Zealand have been used to model GIC in four transformers during two solar storms. Induced electric fields during the storms are calculated from the MT impedances using the magnetic fields measured at the Eyrewell (EYR) geomagnetic observatory, approximately 200 km north of the study area. Calculated GIC during the sudden storm commencements (SSC) give a generally good match to GIC measured by the network operator, Transpower New Zealand. Long period GIC (periods longer than about 10000 s) are less well modelled. Calculations based on thin-sheet modelling, which has restrictions on the shortest period of variation which can be modelled, perform less well for the GIC associated with SSC, but are equally good, if not better, at modeling longer period GIC. Consistent underestimation of large GIC at one transformer (HWBT4) near Dunedin are likely to be the result of uncertainty in the assumed values of line, transformer, and earthing resistances. The assumption of a spatially uniform magnetic field across the study area, which is implied by use of the magnetic field measured at EYR as a basis for calculation, may also lead to incorrect calculation of GIC. For one storm use of magnetic field data from a magnetometer within the study area leads to much improved modelling of the observed GIC. This study compares modelled and measured GIC using specifically measured MT impedance data.

Plain Language Summary

Variations in the Earth’s magnetic field during magnetic storms produce induced currents (geomagnetically induced currents – GIC) in the ground which can present a risk to electricity transmission networks. Long period magnetotelluric measurements made at 62 sites in southern South Island of Aotearoa New Zealand have been used to model GIC observed during two magnetic storms. It is found that large GIC occurring over short periods of time associated with the commencement of a storm can be well modeled. GIC occurring over longer periods are less well modeled. Uncertainty in values of resistances incorporated in the model of the transmission network are likely to be the reason why the size of GIC is consistently underestimated at some locations. The assumption that the magnetic field variations are uniform across the study area is also found to not always be valid.

1 Introduction

On the Earth's surface space weather, originating from activity on the Sun, manifests as geomagnetically induced currents (GIC). These GIC travel along man-made conductive pathways such as electric transmission lines, pipelines, railways and telecommunication cables. In extreme cases GIC can cause communication outages, and damaging transients in electric power grids (Joselyn et al., 1995). The most notable example being the failure of the Hydro-Quebec system during a magnetic storm in 1989 (Boteler, 2019). Quantifying GIC on the Earth's surface requires information about the horizontal geoelectric field induced by the changing magnetic field associated with a geomagnetic storm. The relationship between these is given by the surface impedance (Pirjola, 2005). Several techniques have been used to give surface impedances that may be used in the calculation of GIC. Many calculations (e.g. Boteler, 2001; Wik et al. 2008 ; Myllys et al., 2014; Torta et al., 2014, Marshall et al., 2019) have used simple layered models of electrical conductivity structure to derive the electric fields resulting from the time varying magnetic field. Marshall et al., (2019) also used impedances derived from a 3-dimensional conductivity model to calculate GIC in south-eastern Australia & Kruglyakov et al., (2023) utilized 3D conductivity model to compute GIC along a natural gas pipeline in Fennoscandia. However, two methods have been used to give values of the surface impedance relating electric and magnetic fields.

The first such method involves representing the 3-dimensional conductivity structure of an area by a thin-sheet (TS) model (Vasseur & Weidelt, 1977) in which lateral variations in conductivity are represented by two-dimensional spatial variations in the conductance of a thin-sheet at the surface of an underlying layered electric conductivity profile. This method has been used successfully by, among others, Bailey et al. (2017, 2018) for calculating GIC in the Austrian power network, McKay (2003), Beggan et al. (2013) and Beggan (2015) for the United Kingdom, and extensively in Aotearoa New Zealand by Divett et al. (2017, 2018, 2020) and Mac Manus (2022a, 2022b). It is, however, limited by numerical requirements of the model which restrict the ability to model high frequency electric fields, and hence GIC.

An alternative method for determining the surface impedance is the magnetotelluric (MT) technique (Simpson & Bahr, 2005) in which field measurements of time-varying and electric and magnetic fields are used to directly derive the impedance. MT remains the most efficient geophysical technique for obtaining information about the geoelectrical structure of the Earth from the near surface to depths on the order of 100km. It is limited in frequency range only by the sampling interval employed and the duration of recording. Large scale initiatives to gain geoelectric field coverage across continents have been underway since the mid-2000s, with the EMSCOPE (ElectroMagnetic EarthScope) US MTArray (Schultz, et al., 2006) and Australia Geo-sciences AUSLAMP (Duan, 2021) being two notable examples of magnetotelluric surveys that have been funded by government agencies. Electric field and GIC calculations based on MT measurements have been reported by Bedrosian and Love (2015), Love et al. (2018), Sokolova et al. (2019), Kelbert and Lucas (2020), and Mukhtar et al. (2020).

One limitation on many of the studies of the potential impact of space weather on power networks is the lack of actual measurements of GIC against which to test model calculations. In this regard Aotearoa New Zealand is fortunate in having an over 20-year long archive of GIC measurements on multiple transformers. Increased attention to space weather hazards in Aotearoa New Zealand were initiated by a study analyzing a transformer failure in Dunedin that occurred on 6 November 2001 which was shown to be associated with a change in solar wind dynamic pressure (Marshall et al., 2012). The failure of the transformer was suspected to be due to cumulative deterioration with the 2001 event being the final contributor (Béland and Small, 2004). Such damages initiated the installation by Transpower New Zealand, the network operator, of LT 505-S Liaisons Electroniques-Mécaniques (LEMs) DC monitoring systems at additional substations around the country (MacManus et al., 2017), with a focus on more southern (i.e. poleward) locations. GIC monitoring devices are Hall effect current transducers installed on the transformer neutral line connection to Earth. The devices measure changes in current at a nonuniform sampling rate, with the sampling frequency increasing when a larger change in current is detected.

The resulting archive of monitoring data has been utilized to compare simulated GIC derived from a variety of modeling techniques to observed measurements (Ingham et al., 2017 ; Divett et al. 2017, 2018, 2020 ; Mac Manus et al., 2017, 2022a; Rodger et al., 2017; and Mukhtar et al., 2020). By far the majority of these studies have been based on the thin-sheet technique of Vasseur & Weidelt (1977). A recently completed 62 site MT array study in the south of Aotearoa New Zealand (Ingham et al., 2023) now allows GIC to be modeled using the derived magnetotelluric impedances. In this paper we present the results of this modeling. Mukhtar et al. (2020) have previously presented GIC calculated from MT impedances in the North Island of Aotearoa New Zealand. However, the lack of actual GIC measurements in the North Island during that period meant that calculated GIC could not be compared to actual observations. Although previous studies (e.g. Blake et al., 2016; Torta et al., 2017; Marshall et al., 2019) have used MT data in deriving conductivity models from which GIC have been calculated from model impedances, in this work the GIC are calculated directly from measured MT impedances and are compared to measured GIC (Butala et al., 2017 ; Shetve et al., 2018; EPRI, 2020 ; Kelbert 2020; Cordell et al., 2024). We also compare our results with how well GIC calculated using thin-sheet technique can reproduce measured GIC. In doing so we draw some conclusions as to the advantages and limitations of the two techniques.

In common with other authors (e.g. Beggan, 2015; Dimmock et al. 2019,2020; Marshalko et al. 2021) Divett et al. (2020) found that modeled GIC values are sensitive to the assumed magnetic field variations. In thin-sheet calculations of GIC in southern Aotearoa New Zealand the magnetic field has been assumed to be spatially uniform across the area and represented by measurements from the sole Aotearoa New Zealand geomagnetic observatory at Eyrewell, near Christchurch (Figure 1). We initially make the same assumption for our calculations based on the MT impedances. However, we test the validity of this assumption by also modeling GIC using magnetic field variations recorded at a different location, which, unlike Eyrewell, lies within the spatial extent of the MT array (Figure 1).

We begin by reviewing previous GIC calculations in southern Aotearoa New Zealand before describing the MT data which we use, and the two geomagnetic storms for which we model GIC. After describing the method of calculating induced electric fields from the measured MT impedances, we briefly review the method of using these to calculate GIC in the transmission network. We then present and discuss calculated GIC for the two storms and investigate the effect of basing calculations on magnetic field variations from a recording magnetometer within the study area rather than from the closest geomagnetic observatory which is some 200 km away. Finally, we compare the results to calculations based on the thin-sheet method.

2 GIC studies in Aotearoa New Zealand

As noted earlier, to date GIC studies in Aotearoa New Zealand have largely been based on the use of a thin-sheet conductance model (Vasseur & Weidelt, 1977), although Mukhtar et al. (2020) and Mukhatar (2021) did use limited MT data to compute geoelectric fields. The thin-sheet model uses a numerical model approach to calculate electromagnetic induction at a particular period in a two dimensional thin-sheet of variable conductance overlying a layered conductivity structure. As outlined above, this type of modeling has proven valuable and computationally efficient for regional-scale problems, but makes simplified assumptions about regions where conductivity contrasts may in fact be more complex. Furthermore, the period range is limited due to the main assumptions of the thin-sheet appraoch (Vasseur & Weidelt, 1977. The range of valid periods for the thin-sheet model for the Aotearoa New Zealand region has been calculated as between 5 and 80.5 min (Divett et al., 2020) although Mac Manus et al. (2022a) used a period range of 2 min to 1440 min. The thin-sheet model developed by Divett et al. (2017) covered both North and South Islands of Aotearoa New Zealand and assigned conductance values to the surrounding seas based on bathymetry, and to the land based on a combination of available MT data and geological structure. This version of the thin-sheet model displayed strongest electric fields over most of the South Island's mountainous region consisting of the resistive Southern Alps terrain. Calculations based on the thin-sheet model showed the largest GIC to occur in the transmission lines oriented northwest-southeast, resulting from electric fields primarily influenced by the shape and orientation of the Aotearoa New Zealand continent rather than the direction of the inducing magnetic field (Divett et al., 2017).

Modeling of GIC measured on four transformers during a magnetic storm of 17 March 2015 reported by Divett et al. (2020), showed good agreement with the time variations in GIC but generally underestimated the size of the measured peaks. This was attributed to the inability of the thin-sheet approach to take into account variations faster than about 5 minutes in period. Mac Manus et al. (2022a) subsequently developed a technique of scaling the calculated GIC to give an improved match to observations. This was based on scaling the calculated GIC spectrum for a transformer to match the observed GIC spectrum. The average power spectrum of modeled

GIC calculated using multiple geomagnetic storms (the "local multi-storm corrected power spectrum") was then used as a basis for scaling modeled GIC for a transformer for other storms. The technique was also extended to give a "nationwide multi-storm scaling" which could be applied to any transformer in the Aotearoa New Zealand network, including those on which direct GIC measurements are not made. Although giving a more accurate estimate of peak GIC in most transformers (see, for example, Figure 9 in Mac Manus et al. (2022a)) the technique was still limited by being based only on filtered GIC measurements down-sampled to a 1-minute sampling interval.

3 Historical geomagnetic storms

In this paper we focus on two geomagnetic storms from solar cycle 24: (1) the 17 March 2015 Saint Patrick's Day Storm, and (2) the storm of 07-08 September 2017. The first of these was used by Divett et al. (2020) in presenting results from initial thin-sheet modeling of GIC, while the second was used by Mac Manus et al. (2022a) in illustrating the scaling techniques developed to give an improved fit to the measured GIC.

The Saint Patrick's Day (SPD) 2015 storm was characterized by an interplanetary shock causing a sudden storm commencement (SSC) occurring around 04:46:21 UT. The Earth's magnetic field compression intensified so that by 10:00 UT the storm disturbance (Dst) index dropped to -80nT. Around approximately 11:00 UT, a large magnetic cloud migrated in the opposite direction causing a second storm intensification (Dst = -228nT) on 18 March (Wu et al., 2015). As observed at EYR the SSC was marked by an initial decrease in B_x of 20 nT in around 20 seconds, followed by an increase of nearly 100 nT in 35 seconds, simultaneous with a 60 nT increase in B_y. As is discussed below this resulted in both negative and positive peaks in observed GIC. The subsequent main phase of the storm was characterized by variations in both B_x and B_y including significantly longer periods of over 1 hour.

The second storm for which we calculate GIC occurred during a solar minimum and spanned 07-08 September 2017. A geomagnetic K_p-index of 8 was reached on the 07 September accompanied by a maximum Dst of -33nT (Tassev et al., 2017). Thorough investigation of this storm is highlighted by Clilverd et al. (2018) in which phases of the storm have been identified, three of which fall within the date-range of 07 September to 08 September. The first two events of the storm occurred on the 06 of September and resulted in low magnitude GIC. However, at Eyrewell the SSC just after 23:00 UT on 07 September was marked by a small decrease/increase in B_x/B_y followed by a larger increase/decrease of 80-100 nT over 35 seconds which resulted in triple peaks in observed GIC. As commented by Clilverd et al. (2018), later in the storm, from around 13:00 UT 08 September, the auroral electrojet was at around 48°S and resulted in significant long period variations in the magnetic field.

4 Modeling GIC using MT data

4.1 MT data

The MT data used to model GIC have previously been described by Ingham et al. (2023) who assessed the effect of tectonic and geological structure on the magnitude and orientation of induced electric fields, and hence GIC. The dataset consists of 62 long period MT sites (Figure 1) on a roughly 25 km grid across the Otago and Southland regions of South Island of Aotearoa New Zealand. Prior to these measurements, the majority of MT measurements in the South Island of Aotearoa New Zealand consisted of several profiles (Wannamaker et al., 2002, 2009; Ingham, 1995, 1996) of sites across the central and northern parts of the island, well to the north of the present area of study. Previous measurements were also broadband measurements, covering frequencies much higher than are applicable to GIC, and not extending to such long periods as used in the present study.

Electric and magnetic fields were sampled every second, and analysis of the MT data yielded quality impedances within the period range of 10 - 10000 seconds at practically all sites (Ingham et al., 2023), with shorter and longer period estimates at some sites. The electric fields calculated directly from the MT impedances reflect significantly more complex geoelectric structure than represented in the previous thin-sheet model, and show that induced electric fields are significantly affected by the geologic structure and tectonics of the region (Ingham et al., 2023).

4.2 Geoelectric field computation

Initially, geoelectric fields during the two storms studied were calculated from the magnetotelluric impedances for each site using 1 second magnetic field data from the Eyrewell (EYR) geomagnetic observatory. As discussed previously by Divett et al. (2020) and Mukhtar et al. (2020) the magnetic field variations at Eyrewell (EYR) can be regarded to first-order to be representative of the magnetic field variations across the entire survey region.

The MT impedance tensors ($\underline{Z}$), at 45 discrete frequencies(ω) for each of the 62 sites were filtered to remove outliers. The relationship in the frequency domain between the horizontal electric (E_x, E_y) and magnetic ($\underline{B}$) field components through the four elements of the complex MT impedance tensor,

$$\begin{bmatrix} E_x \\ E_y \end{bmatrix} = \frac{1}{\mu_0} \begin{bmatrix} Z_{xx}(\omega) & Z_{xy}(\omega) \\ Z_{yx}(\omega) & Z_{yy}(\omega) \end{bmatrix} \begin{bmatrix} B_x \\ B_y \end{bmatrix} \quad (1)$$

then allowed the electric field spectra at each site for a given geomagnetic storm be calculated from ($\underline{Z}$) and the EYR magnetic field spectra. To obtain the impedance tensor components at all frequencies a fifth order polynomial was fitted to the variation of each of the real and imaginary components at each site with the logarithm of the period. The polynomial fits were assessed both pre- and post- application of the removal of outliers from the impedance tensor and

R^2 values calculated for both the filtered and unfiltered fits. This showed that in all but a few instances the removal of outliers resulted in an improved fit.

Once the electric field spectra for (E_x, E_y) for a site had been calculated an inverse Fourier Transform was used to obtain the electric field responses to the storm in the time domain. Time series outputs from site 162 for the two storms studied are shown in Figure 2(a) and 2(b).

Prior to GIC computation, the geoelectric fields calculated at each site were interpolated onto a 1/8 x 1/8 degree grid covering the survey area using the nearest neighbor method of interpolation constrained by Delaunay triangulation with fields outside the survey area treated as null. The interpolated field values were stored in 3 dimensional matrices where the x and y components refer to the geoelectric fields (mV/km) and the z component represents time (seconds). For the 17 March 2015 Saint Patrick's Day storm, the electric field during the sudden storm commencement at 04:46:21 UTC are shown in Figure 2(c). The largest electric fields were in the west of the region considered, on the resistive Median Batholith (Figure 1). The peak electric field was between 1 and 2 V/km. This is significantly larger than, and in a very different location to, the peak electric fields of about 0.4 V/km found by Divett et al. (2020) using the thin-sheet model for the same storm period. This is a first indication that the ability of the MT data to represent shorter period variations may lead to significantly larger GIC.

Similarly, the 07 September 2017 storm outputs the largest electric fields during the sudden storm commencement (Figure 2(d)) with, again, the largest electric fields (of between 1.5 and 2.2 V) being in the resistive west of the study area. In both Figures 2(c) and 2(d) larger electric fields also occur close to the south-east coast of the study area, while fields are smaller both on the sediments in the central southern part of the area, and on the Otago Schist (Figure 1), in agreement with the results of Ingham et al. (2023) who calculated the electric field response to uniform magnetic fields across the study area.

4.3 Equivalent circuit grid configuration & GIC computation

As explained by Divett et al. (2017) and Mukhtar et al. (2020), the electrical transmission networks in the North and South Islands of Aotearoa New Zealand are separated by a DC cable under Cook Strait and can be treated as two independent networks. The method of modeling the South Island network at both substation and transformer level has been described in detail by Divett et al. (2018), and the same approach, based on Lehtinen & Pirjola (1985) and Boteler & Pirjola (2014), has been used in this study. As the study area covers only the southern part of the South Island, that part of the network to the north of Roxburgh (ROX in Figure 1) has been treated as an equivalent circuit as described in general by Boteler et al. (2013). As discussed, with specific reference to the south of the South Island by Mukhtar (2020) and Ingham et al. (2023), GIC calculations using the entire South Island network and those representing that part of the network north of ROX by an equivalent circuit show only minor differences in GIC at transformers in the southern South Island. This suggests that GIC at ROX pass to/from ground and no current passes to/from the north. GIC calculated using the thin-sheet technique incorporates the entire South Island and do not make use of the equivalent circuit to represent the part of the network north of Roxburgh.

We model GIC in four transformers. Of these, at Halfway Bush on the edge of Dunedin, is a single-phase transformer HWBT4. The other three transformers are SDNT2 at South Dunedin, INVT5 at Invercargill and MANT6 at Manapouri.

5 Results

5.1 The St. Patrick's Day 2015 storm

GIC resulting from the 2015 Saint Patrick's Day Storm have previously been modeled by Divett et al. (2020), using the thin-sheet model. As indicated above, the magnetic field variations measured at EYR were used as the inducing magnetic field and assumed to be uniform across the study area in both the thin-sheet and MT models. In the case of the MT data, the magnetic field values had a sampling interval of 1 second, while thin-sheet calculations presented here used a sampling interval of 1 minute, following Mac Manus et al. (2022a).

The negative and positive peak values around the sudden storm commencement (SSC) of both the measured GIC and those calculated using the MT data are listed in Table 1. At SDN and HWB the positive peak occurred before the negative peak, while the reverse was true for INV and MAN. Also listed are the unimodular (i.e. negative or positive) peak values resulting from the thin-sheet model described by Divett et al. (2020), and, for further comparison, the peak values from the scaled thin-sheet model as described by Mac Manus et al. (2022a).

The initial peak GIC modeled at SDNT2 and MANT6 modeled using the MT derived electric fields are in good agreement with the measured values. The subsequent model peak GIC of opposite sign are 65-70% of the measured GIC at SDNT2, and 45-55% of the magnitude of the measured values at MANT6. As outlined previously, during the sudden storm commencement, after initial small decreases, B_x increased by about 100 nT over about 35 seconds, while B_y rose by about 60 nT over the same period. It is likely that even with the shortest period of the MT data included in the calculation being somewhat less than 10 s, the electric field response to this rapid change is not fully captured. By comparison, at both HWBT4 and INVT5 negative and positive peak values are underestimated.

The degree to which the MT modeled GIC fit the observed variation in GIC is shown in Figure 3. Not only is there a good match at SDNT2 and MANT6 to the peaks associated with the SSC, but the shape of the subsequent smaller variations is also reproduced. At both HWBT4 and INVT5, although the magnitude of GIC is underestimated, the shape of variations is also generally replicated. The non-uniform sampling rate for the actual GIC measurements is apparent in Figure 3. In general, the sampling rate increases automatically when large changes in GIC are observed but at most locations is never faster than 1 sample every 4 seconds, and in periods of quiescence measurements may be as large as a minute (Clilverd et al., 2020). Also shown are the model GIC calculated from the thin-sheet model as presented by Divett et al. (2020). The larger sampling interval means that only a single broad peak in GIC is modeled and the separate positive and negative peaks are not resolved. The size of this broad peak is generally comparable to that of the principal peak calculated from the MT model, but it lags significantly in time from those in both the MT model and the measured values. It is also noticeable from Table 1 that the scaled model thin-sheet GIC do not give a significantly improved match to the peak GIC at SSC compared to the original thin-sheet GIC. Indeed, for SDNT2 the original thin-sheet calculated GIC are larger. This is due to the scaling being based on average GIC spectra across multiple storms rather than simply specific to the St. Patrick's Day storm.

Divett et al. (2020) commented on the inability of the thin-sheet model to match the large negative GIC at HWBT4 compared to the much better agreement at SDNT2. Halfway Bush, on the hillside on the western edge of Dunedin sits on the volcanic deposits associated with the Dunedin Volcanic Group. South Dunedin, only about 4 km away, lies on soft sediments adjacent to the coast. The two substations thus exist in what are very different environments in terms of ground resistivity. Divett et al. suggested that MT data might give a more accurate representation of the induced electric field near HWB than that provided by the thin-sheet model. However, the MT model, still underestimates the size of the GIC peak.

Measures of how well the MT model GIC fit the observations over this 5-minute time window are given by the correlation coefficient ρ , the performance parameter P as defined by Torta et al. (2014, 2017), and the root-mean-square (rms) misfit of model to observations. Whilst ρ gives a guide to how well the time variations of the two quantities match, P takes into account possible differences in the mean values and standard deviation of the quantities. As noted by Marsal & Torta (2019) even the best models of GIC rarely have $P > 0.5$. Values of both ρ and P have been calculated using the original measured GIC data and the MT model GIC calculated for corresponding times. The calculated values during the SSC are shown in Table 2. As can be seen, correlation coefficients over the SSC are high at HWBT4, SDNT2 and MANT6 reflecting the degree to which the MT model matches the time variation in measured GIC. The root-mean-square misfits (rms), respectively, at these transformers are 13.4 A, 7.1 A and 1.7 A. Although still positive, the correlation at INVT5 is much weaker. Similarly, P values for HWBT4, SDNT2 and MANT6 are high compared to that at INVT5. This lower value arises from the fact that, given the relatively small GIC, the standard deviation of the measured GIC is significantly larger than the root-mean-square (rms) misfit of the model to the data of 4.0 A.

Calculated GIC time series for a 3-hour period later in the St. Patrick's Day storm, from 1300-1600 UT when there were significant longer period variations in observed GIC, are shown in Figure 4. There is a significant difference between transformers in the degree to which the observed GIC are reproduced by the MT model. At SDNT2 and MANT6, the time variations in GIC, both short and long period, are well matched, although magnitudes are slightly underestimated in size. At HWBT4 the time variations in GIC are again well represented, but the size of the modeled GIC is too small. In contrast the MT modeled GIC at INVT5 are small relative to the measurements, and the model does not reproduce the observations well. Noticeably the MT model misses the negative peak in GIC at around 13:20 UT, and gives a small positive peak in GIC at around 15:00 UT when the measurements show a negative peak. As for the SSC the thin-sheet model gives a good fit to the measured GIC at SDNT2 and MANT6, albeit the longer period range means that higher frequency variations are not well captured. At HWBT4 the thin-sheet model almost completely follows the MT model results, whilst at INVT5 the thin-sheet output comparison is worse than that given by the MT model.

The quality of the MT model results is reflected in the ρ and P values shown in Table 2. Between 13:00 and 16:00 the correlation coefficients for HWBT4, SDNT2 and MANT6 are greater than 0.7, but significantly lower for INVT5. P values are lower than for the SSC interval reflecting the higher variability in the observed GIC compared to the model misfit. This is shown by the rms misfits to the observations over this 3-hour period which for HWBT4, SDNT2, INVT5 and MANT6 are 9.25 A, 4.15 A, 1.75 A and 0.86 A respectively. Values of ρ and P for the entire storm window from 03:00-18:00 UT are also shown in Table 2 and as might be expected, yield correlation coefficients and P values that are lower still.

Results from the St. Patrick’s Day 2015 storm thus suggest that the MT model is particularly successful in modeling rapid fluctuations in GIC, and able to broadly reproduce longer period variations. However, there are two significant areas of misfit. At HWBT4 the amplitude of variations is underestimated, and, more problematically, there is an inability to accurately model GIC at INVT5 in time variation, magnitude, or even sign. In this regard Ingham et al. (2023), using a very simplified model of the transmission network, found that GIC at INV were highly dependent on the orientation of the induced electric field and that relatively small changes in this altered the sense of observed GIC. This is discussed further below.

5.2 The 07-08 September 2017 storm

Shown in Figure 5 are modeling results for three of the transformers (SDNT2, HWBT4 and INVT5) for the 1-hour period around the SSC that occurred just after 23:00 UT on 07 September 2017. Results for MANT6 are not shown due to large gaps in the measured GIC data during this event. Measured GIC values at SDNT2 and HWBT4 showed three peaks associated with the SSC – an initial positive peak, followed around 30 seconds later by a negative peak, and then a further positive peak after another 30-45 seconds. At INVT5 the sense of these peaks was reversed although the second negative peak was extremely small. As for the St. Patrick’s Day 2015 storm, and as shown in Table 3, the MT model reproduces the first two of these peaks well for both SDNT2 and HWBT4, but significantly underestimates the third. For INVT5, albeit with much reduced magnitudes, the modeled pattern is also positive-negative-positive, the opposite of the observed GIC. As for the SSC in the St. Patrick’s Day 2015 storm both the initial and scaled thin-sheet models show only a single positive peak which significantly lags in time the second observed positive peak.

Through the rest of the time period shown in Figure 5 the MT model GIC give a very close match to the observed data at SDNT2 and a reasonable one at HWBT4. Although closely following the average value of the GIC at INVT5, the MT model fails to model the sustained negative GIC at INVT5 between about 23:25 and 23:30 UT. Calculation of the correlation coefficients and *P* values over the 1-hour period from 22:45-23:45 UT (Table 4) shows that there is, overall, a negative correlation between the MT-model and GIC at INVT5. A negative *P* value also results. For both SDNT2 and HWBT4 the fits are numerically much better, although it should be noted that the actual rms misfits over this period are similar (3-4 Amps) for all three transformers. The thin-sheet model also fails to model the period of negative GIC at INVT5 and shows relatively little variation in GIC across the whole period. However, the thin-sheet model GIC do provide a reasonable match to the measured data at the other two transformers suggesting better coverage of the longer period storm event.

Measured and modeled GIC for a later period (11:00 – 16:00 UT 08 September) during the storm of 07-08 September 2017 are shown in Figure 6 and show some interesting features. This time interval covers the period when Clilverd et al. (2018) both identified the auroral electrojet as having moved significantly far north and noted that measurements on three separate magnetometers suggested that there were significant small-scale features in the magnetic field variations. This may indicate that the EYR observatory magnetic field data used in calculating the MT electric fields may not be representative of the magnetic field variations across the entire area.

The MT model GIC give a very poor fit to the measured values at INVT5 where, as shown in Table 4, the correlation coefficient and *P* values are both negative. The misfit is particularly noticeable during the interval of 12:00 – 12:45 UT when large negative GIC were observed at INVT5. At HWBT4 the general form of the variations in GIC is reproduced but, again, the magnitude is underestimated. However, there is a much better match to the observed GIC at SDNT2. The thin-sheet model also generally performs poorly at HWBT4 and INVT5, although it, perhaps surprisingly, provides a better fit at SDNT2.

Notwithstanding the inability to fit some of the observations from later on 08 September, these results are broadly similar to those for the 2015 storm and show that, in general, the MT model GIC give a good representation of the GIC variations in the lower South Island observed around a SSC. It can be speculated that reducing the sampling interval would further improve this estimation. Of concern from the southern Aotearoa New Zealand standpoint is the apparent inability to model GIC at INV, although in general these are only of small magnitude. In the following section the poor fit of the MT model to the observed data during 08 September 2017, as seen in Figure 6, is further investigated to assess the effect of choice of representation of the magnetic field variations.

5.3 Effect of assumed magnetic field variations

In all of the models discussed above the magnetic field variations as measured at the Eyrewell (EYR) geomagnetic observatory near Christchurch have been used as a basis for electric field calculations. Although, Divett et al. (2020) suggested that the use of EYR magnetic field variations was reasonable for the St. Patrick's Day 2015 storm when in reality the magnetic field variations are not uniform across the study area. For example, Mukhtar et al. (2020), following Clilverd et al. (2018), quoted that between 12:00 and 13:00 UT on 08 September 2017 the rate of change of the horizontal magnetic field (dH/dt) as measured by a magnetometer near Dunedin was about 31 nT/min compared to a rate of change at EYR of near 12 nT/min. Given that the induced electric field is directly proportional to dH/dt, such spatial variations may indicate the reason why modeling based on EYR magnetic fields does a poor job of replicating GIC during this time interval, especially with regard to modeling the correct sense of GIC at INVT5. It is therefore worth investigating if other magnetic field measurements, rather than those from EYR, improve the calculation of GIC.

The ability to model GIC using a spatially varying magnetic field is generally dependent on the availability of magnetic field measurements from multiple locations that allow techniques such as the use of spherical elementary current systems (SECS) (e.g. Pulkkinen et al. 2003; Wik et al. 2008, Viljanen et al., 2012) to be employed. Given the unavailability of multiple magnetic field measurements in the South Island of Aotearoa New Zealand we, instead, use measurements from a single additional magnetometer located close to Dunedin. The magnetometer, at Swampy Summit (SWA) was installed in 2017 and is a Bartington three-axis magnetic field sensor. The location is only 7 km from the HWB substation (Clilverd et al., 2018). The Swampy magnetometer does not follow observatory standards and the measured data have a uniform sample rate of 0.9771s. For computation of GIC, and comparison with the data recorded at EYR, the magnetic field data were interpolated to give a uniform sampling rate of 1 second. The variations in the horizontal components of the magnetic fields at both SWA and EYR on 07-08 September 2017 are shown in Figure 7. As can be seen, although the initial SSC at around 23:00 on 07 September produced similar changes in magnetic field at EYR and SWA, the later rapid variations in both B_x and B_y near 12:00 on 08 September were significantly larger at Swampy compared to EYR. Clilverd et al. (2018) noted that the peak rate of change of the total horizontal magnetic field, based on 1-minute sampling, associated with this large decrease in field was not only larger at SWA but also occurred slightly earlier.

Geoelectric fields were calculated using the Swampy magnetometer data and the MT impedances in the same manner as for using the EYR magnetic field. The resulting MT model GIC for the two time periods shown in Figures 5 and 6 are shown in Figure 8 for calculations using EYR data (blue lines) and using SWA data (green lines). For the period of 22:55 – 23:35 UT, shown in the left-hand panels, the most noticeable aspect is that the GIC calculated using the Swampy data now give an improved fit to the second positive maximum GIC observed at SDNT2 and HWBT4. There is also an improved fit to this second positive peak at INVT5, while, although smaller than the observed peaks, the two preceding peaks, positive and negative, now also appear. The use of the Swampy magnetometer data also means that negative GIC at INVT5 between about 23:25 and 23:30 UT, which the original MT model did not reproduce, are now included in the model output, albeit as having very small magnitude. The correlation coefficients and *P* values for this time interval, summarized in Table 4 for both the EYR and Swampy models, illustrate the improved fit to the observed GIC for all three transformers.

The right-hand panels of Figure 8 show the modeled GIC for the period 11:00- 16:00 UT on 08 September 2017. This is the period for which Clilverd et al. (2018) reported significant spatial variations in magnetic field and, whereas using the EYR magnetic fields as a basis for modeling did not give a very good fit to the observed GIC, the use of the magnetic field measured at Swampy now results in a significantly better fit. In particular, the large positive GIC at about 12:40 UT are much better replicated at both SDNT2 and HWBT4, as are the subsequent smaller amplitude variations. The GIC model using the Swampy magnetic field also shows slightly negative GIC at INVT5 during the period 12:15-12:45 UT, something that the MT model based on EYR fields did not. However, at INVT5 the size of the model GIC remain significantly smaller than the observed values. This difference between the two Dunedin transformers and INVT5 may well reflect the short scale differences in magnetic field, the Swampy magnetometer being located close to both SDN and HWB, but still some 70 km north and 150 km east of INV. Again, the correlation coefficients and *P* values (Table 4) illustrate the significant improvement in modeling the GIC achieved by using the Swampy magnetic field.

6 Thin-sheet model fits

As can be seen from the results presented above, the principal difference between the two approaches of modeling GIC – that of using directly measured MT impedances compared to the thin-sheet numerical approach, lies in the numerical limitations that the latter imposes on periods (frequencies) that can be modeled. As seen in Figures 3 and 5 and in Tables 1 and 3, the thin-sheet approach is unable to capture rapid fluctuations in GIC occurring on the time-scale of seconds. On the other hand, both approaches generally give a good representation of longer period variations in GIC. Indeed, in some ways, at the longest periods better results are given by the thin-sheet model as there is often increased scatter in the MT impedances at periods longer than about 10^5 s.

Interpolating the observed GIC data to a 1-minute sampling interval using cubic splines allows correlation and *P* values to be calculated for the thin-sheet model, although the difference in time resolution means that a direct comparison of numerical measures of fit with those for the MT approach is not possible. Table 5 shows the ρ and *P* values for three of the time intervals discussed above, both for the original thin-sheet model (Divett et al., 2020) and for the scaled thin-sheet model of Mac Manus et al. (2022a). With the 1-minute sampling the small number of points in the interval 04:45-04:50 UT around the sudden storm commencement on 17 March 2015 makes calculation pointless.

For the two longer period intervals correlation coefficients are high for HWBT4, SDNT2 and MANT6. P values for these transformers also suggest good agreement of the thin-sheet model with the measured data. At INVT5 both ρ and P are negative for both time intervals. As indicated previously the scaled thin-sheet model does not uniformly improve these measures, and at INVT5 makes them significantly worse. Around the SSC of 07 September 2017 the P calculated for SDNT2 is also negative.

7 Discussion

Bedrosian and Love (2015), Love et al. (2018), and Ingham et al. (2023) are examples of studies that have presented the spatial variation of electric fields derived from an array of MT sites measured specifically for the purpose of calculating GIC. The results presented in our study compare GIC modeled through the use of specifically measured MT impedance data with measured GIC. Mukhtar et al. (2020) reported the results of a comparison of MT and thin-sheet GIC calculations in the North Island of Aotearoa New Zealand, but the lack of GIC observations in the North Island prevented comparison with actual measurements. Although our modeling has covered only 2 geomagnetic storms it reveals some salient facts regarding the calculation of GIC using both MT impedance data and the, more commonly used, thin-sheet modeling technique. It also raises questions about the spatial discretization of both thin-sheet models and MT surveys used in modeling GIC.

The largest GIC are generally related to the rapid changes in magnetic field associated with a sudden storm commencement, and frequently involve multiple maxima, separated by a few tens of seconds with changes in the sign of the GIC. The inherent limitation of the thin-sheet approach in modeling high frequency variations means that such changes cannot be modeled using this method. Thin-sheet models typically result in a single maximum value which significantly underestimates the size of the peak GIC (as seen in Figures 3 and 5). The MT approach, although more successful in modeling changes in sign of GIC occurring on the order of seconds, and in reproducing larger GIC, still tends to underestimate the size of the peak GIC. In the current work MT data were measured with a sampling interval of 1 second, such that at some sites impedances estimates with a shortest period of 5-7 seconds are available to be used in GIC modeling. It is possible that a smaller sampling interval, allowing calculation of reliable shorter period impedance estimates might allow better resolution of peak GIC, especially during rapid changes of magnetic field such as during a SSC.

In contrast, whereas the thin-sheet technique is numerically limited in terms of representing short period variations, the MT method is dependent on the reliability of transfer function estimates. The short period cut-off of around 5-7 seconds may be responsible for underestimating GIC associated with a sudden storm commencement, while less reliable calculation of impedance tensors at the longest periods possibly effects calculation of longer period GIC. The longest period at which reliable estimates can be obtained depends on the duration of recording (~1 month in the current study) and the level of magnetic activity over this period. As quoted above reliable estimates at the majority of sites in this study extended to

~10000 seconds period, with longer estimates at a smaller number of sites. Given the smoothing and interpolation of estimates onto a 1/8 of a degree grid, it is likely therefore that the MT model GIC will not reflect variations of longer than, at most, 10000 s. The numerical calculation of induced electric fields in the thin-sheet technique does not suffer from this limitation and may, therefore, give better calculation of longer period GIC.

Long-lasting sustained GIC has been shown to saturate transformer cores and produce harmonic distortion (e.g., Clilverd et al., 2018; Rodger et al., 2020). The occurrence of smaller but much longer lasting GIC may lead to degradation of transformers (Gaunt & Coetzee, 2007; Gaunt, 2014). As can be seen from Figures 4 and 6, both the thin-sheet and MT approaches are able to model such longer period fluctuations at some locations but are manifestly unable to do so at others. This raises the question of why this discrepancy occurs.

One potential reason for this is the assumption of spatially uniform magnetic field variations across the study area. In Aotearoa New Zealand this assumption is enforced by the existence of only a single geomagnetic observatory, some 200 km north-east of the current area of interest. Although, in the present case this assumption appears to be reasonably successful in modeling of GIC, it must be questioned as to how applicable it will be for use in future GIC calculations. For example, in the north of the North Island of Aotearoa New Zealand, some 800 km north of the Eyrewell observatory. As was illustrated in a previous section, the use of magnetic field variations from a proximal location can notably improve GIC calculations (at least using the MT method) at sites close to the magnetometer location, but still does not allow for rapid spatial variations in the magnetic field. A possible method of overcoming this limitation is suggested below.

It is also pertinent that model GIC calculated using both MT impedances and thin-sheet modelling consistently underestimate the magnitude of GIC at some locations, in particular, as evidenced above, HWBT4 and INVT5. In this regard calculation of GIC is very dependent on the correct representation of the power grid configuration, including the resistances of power lines, earthing points, and transformers that are used in the model calculations. The fact that both MT and thin-sheet model calculations tend to do well at fitting the same transformers, but poorly at fitting others, suggests that this may have some significance. Divett et al. (2018) gave a detailed explanation of how these parameters are included in the power network modeling, whilst Divett et al. (2020) presented the results of sensitivity testing of the importance of various parameters. This was done by running thin-sheet calculations with different input parameters and comparing the calculated GIC power spectrum with that for a base model. One such test used a simplified network in which combined transformer resistance and resistance to ground were assumed to be 0.5 Ω. As an example of the impact of these changes results were given for SDNT2 and it was found that for this transformer the calculated GIC spectrum was reduced by 40%. This was attributed to the fact that the actual transformer resistance was 0.23 Ω and the earthing resistance only 0.03 Ω, so that the combined change to 0.5 Ω effectively doubled the resistance. However, it was found that at another transformer elsewhere in the network the GIC power spectrum increased by a factor of 10. Incorrect values related to the topology of the network therefore remain the most likely reason why GIC are underestimated for some substations/transformers.

This issue is also potentially complicated by the fact that values of these parameters may change with time. For example, many studies have looked into the effect of aging on the insulation within a transformer (e.g. Du et al.,1999; Martin et al.,2013; Cui et al., 2016; Wang et al., 2018). In particular, Risos (2018), Risos & Gouws (2019), and Abdi et al. (2023) have noted that the conductivity of insulating oil increases markedly with age. The magnitude of this effect depends on heating of the oil and, as noted by Clilverd et al. (2018), temperature increases in a transformer are affected by the magnitude and duration of GIC. Although, insulating oil in a transformer has a very high resistance, it does potentially provide a parallel current path to the transformer windings and it is conceivable that degradation of the oil as it ages may impact the overall resistance of a transformer. The earthing resistance of a transformer may also vary temporally with long-term changes to ground conditions also influencing GIC computations.

8 Representing spatial variations in the magnetic field

As indicated above, the assumption that variations in the magnetic field are uniform across the study area may lead to erroneous calculation of GIC. The existence of only a single geomagnetic observatory in Aotearoa New Zealand means that alternative methods to account for this are required compared to situations where multiple observatories exist, stressing the importance of this increase with distance of the study area from the observatory. The use of inter-station transfer functions is suggested as a means of dealing with this issue.

Inter-station transfer functions have previously been discussed in other contexts by, for example, Wang et al. (2017) and Sato et al. (2020). For use in calculating more realistic electric fields for use in modeling GIC from MT data, the following procedure is suggested. Estimation of the long-period MT impedance at a site is based on the measurement of electric and magnetic fields at the site for over a period of about a month, with the electric and magnetic fields represented by equation (1). More explicitly, remembering that all quantities are functions of frequency:

$$\begin{aligned} E_x^i &= \frac{1}{\mu_0}\left[Z_{xx}^i B_x^i + Z_{xy}^i B_y^i\right] \\ E_y^i &= \frac{1}{\mu_0}\left[Z_{yx}^i B_x^i + Z_{yy}^i B_y^i\right] \end{aligned} \tag{2}$$

where the superscripts *i* indicate fields and impedance tensor elements at the *i*th site. For the month of recording, the measured magnetic fields at a site may be related to those measured at the local (in this case, EYR) observatory (B_x^E and B_y^E)through transfer functions *J*, *K*, *L* and *M*, calculated in the manner given by Ingham et al. (2017). Then

$$\begin{aligned} B_x^i &= J^i B_x^E + K^i B_y^E \\ B_y^i &= L^i B_x^E + M^i B_y^E \end{aligned} \tag{3}$$

and electric fields to be used in modeling GIC can be calculated from the observatory magnetic field variations from

$$E_x^i = \frac{1}{\mu_0}\left[\left(Z_{xx}^i J^i + Z_{xy}^i L^i\right)B_x^E + \left(Z_{xx}^i K^i + Z_{xy}^i M^i\right)B_y^E\right]$$
$$E_y^i = \frac{1}{\mu_0}\left[\left(Z_{yx}^i J^i + Z_{yy}^i L^i\right)B_x^E + \left(Z_{yx}^i K^i + Z_{yy}^i M^i\right)B_y^E\right] \quad (4)$$

The transfer functions *J*, *K*, *L* and *M* for a site thus incorporate any spatial differences in the magnetic field. Future work could entail incorporating the magnetic variation with the GIC models but remains outside the scope of this particular study.

8 Conclusions

In presenting the results of GIC calculations from MT impedance tensors measured at 62 sites in southern Aotearoa New Zealand we have identified advantages and limitations in modeling GIC through either MT impedances or the thin-sheet numerical technique. Specifically:

(1) Modeling using MT impedance tensors is better able to represent short period variations in GIC associated with, for example, a sudden storm commencement.

(2) Modeling of long period GIC variations is limited using MT impedances by how well the impedance tensor elements can be estimated at longer periods. Long period GIC calculated through the thin-sheet method are limited only by the accuracy of the thin-sheet representation.

(3) For both methods allowing for the non-uniformity of magnetic field variations across a study area is important which is proven by using a magnetometer closer to the study region.

(4) All calculations are limited by the accuracy of the power grid resistance data incorporated in the calculation of GIC. This finding is supported by the fact that GIC models computed via two separate methods during 2 geomagnetic storms yield poor correlations to measured GIC at HWBT4 and INVT5, suggesting that the power grid configuration values are a culprit for underestimated GIC.

Acknowledgments

This research, including scholarship funding for lead author, was supported by the Aotearoa New Zealand Ministry of Business, Innovation and Employment (MBIE) Endeavor Fund Research Program contract UOOX2002. The authors thank the Institute of Geological and Nuclear Sciences Limited (GNS), for supporting the MT field data acquisition.

Open Research

Magnetotelluric data used in this paper can be requested at the GNS Science Dataset Catalogue (GNS Science, 2021).

The EYR magnetic field data were obtained via the open source Intermagnet data portal (INTERMAGNET, et al., 2020); (INTERMAGNET, et al., 2021).

The SWP magnetic field data were collected by University of Otago Department of Physics and can be requested therein (Brundell J., et al., 2017).

The New Zealand electrical transmission network's DC characteristics and DC measurements were provided by Transpower New Zealand with caveats and restrictions. This includes requirements of permission before all publications and presentations and no ability to provide the observations themselves. In addition, we are unable to provide the New Zealand network characteristics due to commercial sensitivity. Requests for access to these characteristics and the DC measurements need to be made to Transpower New Zealand. At this time, the contact point is Michael Dalzell (Michael.Dalzell@transpower.co.nz).

Figure 1 was constructed in QGIS 3.20 (QGIS.org, 2023). Figure 2 a-d were compiled with Matplotlib 3.8.0 (Hunter, 2007). Figures 3-8 were made with Matlab version R2022A (The MathWorks Inc., 2022).

References

Abdi, S., A.M. Haddad, N. Harid & A. Boubakeur, A. (2023). Modeling the effect of thermal aging on transformer oil electrical characteristics using a regression approach. *Energies*, 16, 381.doi:10.3390/en16010381

Bailey, R. L., Halbedl, T. S., Schattauer, I., Achleitner, G., & Leonhardt, R. (2018). Validating GIC models with measurements in Austria: Evaluation of accuracy and sensitivity to input parameters. *Space Weather*, *16*, 887–902. doi.org/10.1029/2018SW001842

Bailey, R. L., Halbedl, T. S., Schattauer, I., Römer, A., Achleitner, G., Beggan, C. D., et al. (2017). Modeling geomagnetically induced currents in midlatitude central Europe using a thin-sheet approach. *Annales Geophysicae*, *35*, 751–761, doi:10.5194/angeo-35-751.

Bedrosian, P.A. & J.L. Love (2015). Mapping geoelectric fields during magnetic storms: synthetic analysis of empirical United States impedances. *Geophys. Res. Lett.*, *42*, 10,160–10,170.doi:10.1002/2015GL066636.

Beggan, C. (2015). Sensitivity of geomagnetically induced currents to varying auroral electrojet and conductivity models. *Earth Planets and Space*, 67, 1-12.doi:10/1186/s40623-014-0168-9.

Beggan, C. D., Beamish, D., Richards, A., Kelly, G. S., & Thomson, A. W. (2013). Prediction of extreme geomagnetically induced currents in the UK high-voltage network. *Space Weather*, *11*, 407–419. doi.org/10.1002/swe.20065

Béland, J. & K. Small (2004). Space Weather Effects on Power Transmission Systems: The Cases of Hydro-Québec and Transpower New ZealandLtd. In: Daglis, I.A. (eds) Effects of Space Weather on Technology Infrastructure. NATO Science Series II: Mathematics, Physics and Chemistry, vol 176. Springer, Dordrecht, doi:10.1007/1-4020-2754-0_15.

Blake, S. P., P. T. Gallagher, J. McCauley, A. G. Jones, C. Hogg, J. Campanya, C. Beggan, A. W. P. Thomson, G. S. Kelly, and D. Bell (2016), Geomagnetically induced currents in the Irish power network during geomagnetic storms, *Space Weather*, 14, 1136–1154.doi:10.1002/2016SW001534.

Boteler, D.H. (2001). Assessment of geomagnetic hazard to power systems in Canada. *Natural Hazards*, 23, 101-120.doi:10.1023/A:1011194414259.

Boteler, D.H. (2019). A 21st Century view of the March 1989 magnetic storm. *Space Weather*, 17, 1427–1441.doi:10.1029/2019SW002278.

Boteler D.H., A.J.C. Lackey, L. Marti and S. Shelemy (2013). Equivalent circuits for modeling geomagnetically induced currents from a neighbouring network. *2013 IEEE Power & Energy Society General Meeting*, Vancouver, BC, Canada, 2013, pp. 1-5.doi:10.1109/PESMG.2013.6672982.

Boteler, D. & R. Pirjola (2014). Comparison of methods for modeling geomagnetically induced currents. *Annales Geophysicae*, 32, 1177-1187.doi:10.5194/angeo-32-1177-2014.

Brundell J., & Otago University Department of Physics (2017). SWAMPY Magnetometer Data. [Dataset]. doi.org/10.6084/m9.figshare.25669749

Butala, M. D., Kazerooni, M., Makela, J. J., Kamalabadi, F., Gannon, J. L., Zhu, H., & Overbye, T. J. (2017). Modeling geomagnetically induced currents from magnetometer measurements: Spatial scale assessed with reference measurements. Space Weather, 15(10), 1357-1372.

Clilverd, M. A., C.J. Rodger, J.B. Brundell, M. Dalzell, I. Martin, D.H. Mac Manus & Y. Obana (2018). Long-lasting geomagnetically induced currents and harmonic distortion observed in New Zealand during the 7–8 September 2017 disturbed period. *Space Weather*, *16*(6), 704-717, doi:org/10.1029/2018SW001822.

Clilverd, M. A., Rodger, C. J., Brundell, J. B., Dalzell, M., Martin, I., Mac Manus, D. H., & Thomson, N. R. (2020). Geomagnetically induced currents and harmonic distortion: High time resolution case studies. *Space Weather*, 18, doi.org/10.1029/2020SW002594

Cordell, D., Mann, I. R., Parry, H., Unsworth, M. J., Cui, R., Clark, C., ... & MacMullin, R. (2024). Modeling geomagnetically induced currents in the Alberta power network: Comparison and validation using Hall probe measurements during a magnetic storm. Space Weather, 22(4), e2023SW003813.

Cui, Y., H. Ma, T. Saha, C. Ekanayake & D. Martin (2016). Moisture-dependent thermal modeling of power transformer. *IEEE Transactions on Power Delivery*, 31 (5), 2140-2150.doi: 10.1109/TPWRD.2016.2569123.

Dimmock, A. P., L. Rosenqvist, J.-O.Hall, A. Viljanen, E. Yordanova, I. Honkonen, M. Andre & E.C. Sjöberg (2019). The GIC and geomagnetic response over Fennoscandia to the 7–8

September 2017 geomagnetic storm. *Space Weather*, 17, 989–1010.doi:10.1029/2018SW002132.

Dimmock, A. P., L. Rosenqvist, D.T. Welling, A. Viljanen, I. Honkonen, R.J. Boynton & E. Yordanova (2020). On the regional variability of dB/dt and its significance to GIC. *Space Weather*,18, e2020SW002497.doi:10.1029/2020SW002497.

Divett, T., M. Ingham, C.D. Beggan, G.S. Richardson, C.J. Rodger, A.W.P. Thomson & M. Dalzell, (2017). Modeling geo-electric fields and geomagnetically induced currents (GIC) around New Zealand to explore GIC in the South Islands's electrical transmission network. *Space Weather*, 15, 1396-1412.doi:10.1002/2017SW001697.

Divett, T., G.S. Richardson, C.D. Beggan, C.J. Rodger, D.H. Boteler, M. Ingham, D.H. MacManus, A.W.P. Thomson, & M. Dalzell (2018). Transformer-level modelingof geomagnetically induced currents in New Zealand's South Island. *Space Weather*, 16, 718–735.doi: 0.1029/2018SW001814.

Divett, T., D.H. Mac Manus, G.S. Richardson, C.D. Beggan, C.J. Rodger, M. Ingham, E. Clarke, A.W.P. Thomson, M. Dalzell & Y. Obana (2020). Geomagnetically induced current model validation from New Zealand's South Island. *Space Weather*.,18, e2020SW002494.doi: 10.1029/2020SW002494.

Du, Y., M. Zahn, B. C. Lesieutre, A. V. Mamishev & S. R. Lindgren (1999). Moisture equilibrium in transformer paper-oil systems. *IEEE Electrical Insulation Magazine*, 15 (1), 11-20.doi: 10.1109/57.744585.

Duan, J. (2021). Electrical resistivity structures and mineral prospectivity from exploring for the future AusLAMP data (2016-2019) in northern Australia. RECORD 2021/021, Geoscience Australia, Canberra.doi:10.11636/Record.2021.021.

Gaunt, C.T. (2014). Reducing uncertainty – responses for electricity utilities to severe solar storms. *Journal of Space Weather and Space Climate*, 4, A01.doi:10/1051/SWSC/2013058.

Gaunt, C.T. & G. Coetzee (2007). Transformer failures in regions incorrectly considered to have low GIC-risk. IEEE PowerTech, Lausanne, 807-812.doi:10.1109/PCT.2007.4538419.

GNS Science. (2021). Magnetotellurics [Data set]. GNS Science. https://doi.org/10.21420/0KY8-MX13

Hunter, J. D. (2007). "Matplotlib: A 2D Graphics Environment", Computing in Science & Engineering, vol. 9, no. 3, pp. 90-95. [Software]. DOI 10.5281/zenodo.8347255.

Ingham, M. (1995). Electrical structure along a transect of the central South Island, New Zealand. *New Zealand Journal of Geology and Geophysics,* 38, 559-563.doi: 10.1080/00288306.1995.9514683.

Ingham, M. (1996). Magnetotelluric soundings across the South Island of New Zealand: electrical structure associated with the orogen of the Southern Alps. *Geophysical Journal International*, 124, 134-148.doi: 10.1111/j.1365-246X.1996.tb06358.x.

Ingham M, C.J. Rodger, T. Divett, M. Dalzell & T. Petersen (2017). Assessment of GIC based on transfer function analysis. *Space Weather*, 15, 1615–1627.doi:10.1002/2017SW001707.

Ingham, M., K. Pratscher, W. Heise, E. Bertrand, M. Kruglyakov & C.J. Rodger (2023). Influence of tectonic and geological structure on GIC in southern South Island, New Zealand. *Space Weather*, 21, e2023SW003550.doi: 10.1029/2023SW003550.

INTERMAGNET, et al. (2020). Global magnetic observatory data 1991 - 2015. [Dataset]. GFZ Data Services. https://doi.org/10.5880/INTERMAGNET.1991.2015

INTERMAGNET, et al. (2021). Intermagnet Reference Data Set (IRDS) 2017 – Definitive Magnetic Observatory Data [Data set]. GFZ Data Services. https://doi.org/10.5880/INTERMAGNET.1991.2017

Joselyn, J., G. Heckman, & R. Zwickl (1995). The Space Weather Program at the NOAA Space Environment Center. Space Programs and Technologies Conference. AIAA 1995-3569. *Space Programs and Technologies Conference.* American Institute of Aeronautics and Astronautics, doi:10.2514/6.1995-3569.

Kelbert, A. (2020). The role of global/regional earth conductivity models in natural geomagnetic hazard mitigation. Surveys in Geophysics, 41(1), 115-166.

Kelbert, A. & G.M. Lucas (2020). Modified GIC estimation using 3-D earth conductivity. *Space Weather*, *18*, e2020SW002467.doi:10.1029/2020SW002467.

Kruglyakov, M., Marshalko, E., Kuvshinov, A., Smirnov, M., & Viljanen, A. (2023). Multi-site transfer function approach for real-time modeling of the ground electric field induced by laterally-nonuniform ionospheric source. Space Weather, 21, e2023SW003621.doi:10.1029/2023SW003621

Lehtinen, M. & R. Pirjola (1985). Currents produced in earthed conductor networks by geomagnetically-induced electric fields. *Annales Geophysicae*, 3, 479–484.

Love, J.J., G.M. Lucas, A. Kelbert & P. Bedrosian (2018). Geoelectric hazard maps for the Mid-Atlantic United States: 100 year extreme values and the 1989 magnetic storm. *Geophysical Research Letters*, 45, 5-14.doi:10.1002/2017GL076042.

Mac Manus, D. H., C.J. Rodger, M. Dalzell, A.W. Thomson, M.A. Clilverd, T. Petersen, Wolf, M.M., Thomson, N.R. & Divett, T. (2017). Long-term geomagnetically induced current observations in New Zealand: Earth return corrections and geomagnetic field driver. *Space Weather*, *15*, 1020-1038.doi: 10.1002/2017SW001635.

Mac Manus, D. H., C.J. Rodger, M. Ingham, M.A. Clilverd, M. Dalzell, T. Divett, G.S. Richardson & T. Petersen (2022a). Geomagnetically induced current model in New Zealand across multiple disturbances: Validation and extension to non-monitored transformers. *Space Weather*, 20, e2021SW002955.doi:10.1029/2021SW002955.

Mac Manus, D. H., C.J. Rodger, M. Dalzell, A. Renton, G.S. Richardson T. Petersen & M.A. Clilverd, (2022b). Geomagnetically induced current model in New Zealand: extreme storm analysis using multiple disturbance scenarios and industry provided hazard magnitudes. *Space Weather*, 20, e2022SW003320.doi:10.1029/2022SW003320.

Marsal, S. & J.M. Torta (2019). Quantifying the performance of geomagnetically induced current models. *Space Weather*, 17(7), 941–949, doi:10.1029/2019SW002208.

Marshall, R.A., M. Dalzell, C.L. Waters, P. Goldthorpe & E.A. Smith (2012). Geomagnetically induced currents in the New Zealand power network, *Space Weather*, 10, S08003, 0.1029/2012SW000806.

Marshall, R.A., L. Wang, G.A. Paskos, G. Olivares-Pulido, T. Van der Walt, C. Ong, D. Mikkelsen, G. Hesse, B. McMahon, E. Van Wyk, G. Ivanovich, D. Spoor, C. Taylor & A. Yoshikawa (2019). Modeling geomagnetically induced currents in Australian power networks using different conductivity models. *Space Weather*, 17, 727-756.doi:10.1029/2018SW002047.

Marshalko, E., M. Kruglyakov, A. Kuvshinov, I. Juusola, N.K. Kwagala, E. Sokolova & V. Pilipenko (2021). Comparing three approaches to the inducing source setting for the ground electromagnetic field modeling due to space weather events. *Space Weather*, 19, e2020SW002657.doi:10.1029/2020SW002657.

Martin, D., C. Perkasa & N. Lelekakis (2013). Measuring paper water content of transformers: a new approach using cellulose isotherms in nonequilibrium conditions. *IEEE Transactions on Power Delivery*, 28 (3), 1433-1439.doi: 10.1109/TPWRD.2013.2248396.

The MathWorks Inc. (2022). MATLAB version: 9.13.0 (R2022a), Natick, Massachusetts. [Software]. The MathWorks Inc https://www.mathworks.com

McKay, A. J. (2003). Geoelectric fields and geomagnetically induced currents in the United Kingdom (PhD Thesis). Retrieved from (https://era.ed.ac.uk/handle/1842/639). University of Edinburgh.

Mortimer, N., F. Davey, A. Melhuish, J. Yu & N.J. Godfrey (2002). Geological interpretation of a deep seismic reflection profile across the eastern Province and Medial Batholith, New Zealand: crustal architecture of an extended Phanerozoic convergent margin. *New Zealand Journal of Geology and Geophysics*,45,349-363.doi:10.1080/00288306.2002.9514978.

Mukhtar, K. (2021). Geomagnetically induced currents in the New Zealand power system. Unpublished PhD Thesis, Victoria University of Wellington, pp. 285, https://openaccess.wgtn.ac.nz/articles/thesis/Geomagnetically_induced_currents_inThe_New_Zealand_power_system/15144096/1.

Mukhtar, K., M. Ingham, C.J. Rodger, D.H. Mac Manus, T. Divett, W. Heise, E. Bertrand, M. Dalzell, M. & T. Petersen (2020). Calculation of GIC in the North Island of New Zealand using MT data and thin-sheet modeling. *Space Weather*, 18, e2020SW002580.doi: 10.1029/2020SW002580.

Myllys, M., A. Viljanen, O.A. Rui & T.M. Ohnstad (2014). Geomagnetically induced currents in the Norway: the northernmost high-voltage power grid in the world. *Journal of Space Weather and Space Climate*, 4, A10.doi:10/1051/swsc/2014007.

Pirjola, R. (2005). Effects of space weather on high-latitude ground systems. *Advances in Space Research*, 36, 2231-2240.doi: 10.1016/j.asr.2003.04.074.

Pulkkinen, A., O. Amm, A. Viljanen, and BEAR Working Group (2003), Ionospheric equivalent current distributions determined with the method of spherical elementary current systems, *J. Geophys. Res.*, **108**(A2), 1053.doi:10.1029/2001JA005085.

QGIS.org (2023). QGIS Geographic Information System. Open Source Geospatial Foundation Project [Software]. http://qgis.org.

Risos, A. (2018). The Physics of Interdigitated Dielectrometry Sensors and Application as In-Situ Oil Oxidation Monitoring. PhD Thesis, Victoria University of Wellington, pp. 189, https://openaccess.wgtn.ac.nz/articles/thesis/The_Physics_of_Interdigitated_Dielectrometry_Sensors_and_Application_as_In-Situ_Oil_Oxidation_Monitoring/17152115.

Risos, A. & G. Gouws (2019). In-situ aging monitoring of transformer oil via the relative permittivity and DC conductivity using novel interdigitated dielectrometry sensors (IDS). *Sensors and Actuators B: Chemical*, 287, 602-610.doi :10.1016/j.snb.2018.12.037.

Rodger, C. J., D.H. Mac Manus, M. Dalzell, A.W. Thomson, E. Clarke, T. Petersen, M.A. Clilverd, & T. Divett (2017). Long-term geomagnetically induced current observations from New Zealand: Peak current estimates for extreme geomagnetic storms. *Space Weather*, *15*, 1447-1460.doi:10.1002/2017SW001691.

Rodger, C. J., Clilverd, M. A., Mac Manus, D. H., Martin, I., Dalzell, M., Brundell, J. B., et al. (2020). Geomagnetically Induced Currents and Harmonic Distortion: Storm-time Observations from New Zealand. Space Weather, 18, e2019SW002387. doi.org/10.1029/2019SW002387.

Sato, S., Tn. Goto & K. Koike (2020). Spatial gradients of geomagnetic temporal variations causing the instability of inter-station transfer functions. *Earth Planets and Space*, 72, 105.doi: 10.1186/s40623-020-01231-0

Schultz, A., G.D. Egbert, A. Kelbert, T. Peery, V. Clote, B. Fry, S. Erofeeva, S., & Staff of the National Geoelectromagnetic Facility and their contractors (2006). *USArray magnetotelluric transfer functions*. doi.org/10.17611/DP/EMTF/USARRAY/TA.

Shetve, K. S., Birchfield, A. B., Lee, R. H., Overbye, T. J., & Gannon, J. L. (2018, October). Impact of 1D vs 3D Earth conductivity based electric fields on geomagnetically induced currents. In 2018 IEEE PES innovative smart grid technologies conference Europe (ISGT-Europe) (pp. 1-6). IEEE.

Simpson, F. & K. Bahr (2005). Practical magnetotellurics. Cambridge University Press.doi:10/1017/CBO9780511614095.

Sokolova, E.Y., O.V. Kozyreva, V.A. Pilipenko, Y.A. Sakharov & D.V. Epishkin (2019). Space-weather-driven geomagnetic- and telluric-field variability in northwestern Russia in correlation with geoelectrical structure and currents induced in electric-power grids. *Izvestiya Atmospheric and Oceanic Physics*, 55, 1639–1658.doi.10.1134/S000143381911015X.

Tassev, Y., P. Velinov, L. Mateev & D. Tomova (2018). Analysis of extreme solar activity in early September 2017: G4 - severe geomagnetic storm (07-0809) and GLE72 (1009) in solar minimum. *Comptes Rendus de l'Academie Bulgare des Sciences*, 70(10), 1437-1444.

Torta, J.M., S. Marsal & M. Quintana (2014). Assessing the Hazard from geomagnetically induced currents to the entire high-voltage power network in Spain. *Earth, Planets and Space*, 66, 87.doi: 10.1186/1880-5981-66-87.

Torta, J.M., A. Marcuello, J. Campanya, S. Marsal, P.Queralt % J. Ledo (2017). Improving the modeling of geomagnetically induced currents in Spain. *Space Weather*, 15, 691-703.doi: 10.1002/2017SW001628.

Use of Magnetotelluric Measurement Data to Validate/Improve Existing Earth Conductivity Models. EPRI, Palo Alto, CA: 2020. 3002019425; https://www.epri.com/research/products/000000003002019425 .

Vasseur, G., & P. Weidelt (1977). Bimodal electromagnetic induction in non-uniform thin sheets with an application to the northern Pyrenean induction anomaly. *Geophysical Journal International*, 51, 669–690.doi : 10/1111/j.1365-246X.1977.tb04213x.

Viljanen, A., R. Pirjola, M. Wik, A. Adam, E, Prácser, Y. Sakharov and J. Katkalov (2012). Continental scale modeling of geomagnetically induced currents. *J. Space Weather Space Clim.*, 2, A17.doi:10.1051/swsc/2012017.

Wang, H., J. Campanyà, J. Cheng, G. Zhu,W. Wei, S. Jin, & G. Ye (2017). Synthesis of natural electric and magnetic time-series using inter-station transfer functions and time-series from a neighboring site (STIN): applications for processing MT data. *Journal of Geophysical Research Solid Earth*,122, 5835–5851,doi:10.1002/2017JB014190.

Wang, D., L. Zhou, A. Wang, H. Li, W. Liao, L. Guo & Y. Cui (2018). Effects of thermal aging on moisture diffusion in insulation paper immersed with mineral oil. *IEEE Transactions on Dielectrics and Electrical Insulation*, 25 (5), 1888-1896.doi: 10.1109/TDEI.2018.007239.

Wannamaker, P. E., G.R. Jiracek, J.A. Stodt, T.G. Caldwell, V. Gonzalez, J.D. McKnight & A.D. Porter (2002). Fluid generation and pathways beneath an active compressional orogen, the

New Zealand Southern Alps, inferred from magnetotelluric data. *Journal of Geophysical Research*, 107, 1–20.doi:10.1029/2001JB000186.

Wannamaker, P., T. Caldwell, G. Jiracek, V. Maris, G.J. Hill, Y. Ogawa, H.M. Bibby, S.L. Bennie & W. Heise (2009). Fluid and deformation regime of an advancing subduction system at Marlborough, New Zealand. *Nature*, 460, 733–736.doi:10.1038/nature08204.

Wik, M., A. Viljanen, R. Pirjola, A. Pulkkinen, P. Wintoft and H. Lundstedt (2008). Calculation of geomagnetically induced currents in the 400 kV power grid in southern Sweden. *Space Weather*, 6, S07005.doi: 0.1029/2007SW000343.

Wu, CC., K. Liou, R.P. Lepping, L. Hutting, S. Plunkett, R.A. Howard & D. Socker (2015).. The first super geomagnetic storm of solar cycle 24: The St. Patrick's day event (17 March 2015). *Earth Planets and Space*, 68, 151.doi:10.1186/s40623-016-0525-y.

Figure 1: Locations of the 62 magnetotelluric sites in the southernmost part of the Aotearoa South Island, New Zealand superimposed on the tectonic map amended from Mortimer et al. (2002). Observed GIC measurement locations discussed in the text are denoted by the red stars. Transmission lines are shown by the blue lines. The yellow star denotes the location of the Eyrewell observatory near Christchurch and the green star denotes the location of the SWAMPY magnetometer near Dunedin. Map modified from Ingham et al., 2023.

Figure 2: Electric field time series at site 162 for (a) 17 March 2015, and (b) 07-08 September 2017. Panels (c) and (d) show maps of the interpolated electric fields across the survey area at the sudden storm commencement marked by the large spike in electric fields in (a) and (b).

Figure 3: Observed and model GIC around the sudden storm commencement of the St. Patrick's Day 2015 storm. Red dots denote observed values, the blue lines show the model values calculated from the MT impedances with a time spacing of 1 second, black diamonds are the 1-minute interval GIC calculated from the TS model (Divett et al., 2020).

Figure 4: Measured and model GIC between 1300 and 1600 UT on 17 March 2015. Red dots denote observed values, the blue lines show the model values calculated from the MT impedances with a time spacing of 1 second, black diamonds are the 1-minute interval GIC calculated from the TS model (Divett et al., 2020).

Figure 5: Measured and model GIC for 22:55 – 23:35 UT on 07 September 2017. Red dots denote observed values, the blue lines show the model values calculated from the MT impedances with a time spacing of 1 s, black diamonds are the 1-minute interval GIC calculated from the TS model (Divett et al., 2020).

Figure 6: Measured and model GIC for 1100 – 1600 UT on 08 September 2017. Red dots denote observed values, the blue lines show the model values calculated from the MT

impedances with a time spacing of 1 s, black diamonds are the 1-minute interval GIC calculated from the TS model (Divett et al., 2020).

Figure 7: Variations in the horizontal components of the magnetic field between 18:00 UT on 07 September 2017 and 21:00 on 08 September 2017 recorded at Swampy Summit (SWA) and the Eyrewell (EYR) geomagnetic observatory.

Figure 8: Measured and model GIC for both 22:45 – 23:45 UT on 07 September 2017 (left-hand panels) and 11:00 – 16:00 UT on 08 September 2017 (right-hand panels). Model values are calculated using magnetic fields measured at EYR (blue lines) and SWA (green lines). Red dots denote observed values.

Table 1: Minimum and maximum values (in Amps) of transformer GIC during the SSC of the St. Patrick's Day 2015 Storm.

Table 2: Correlation coefficient (ρ) and *P* values between MT model GIC and measured GIC for each transformer considered during 3 intervals of time during the 17 March 2015 storm.

Table 3: Minimum and maximum values (in Amps) of transformer GIC during the SSC at ~2300 07 September 2017.

Table 4: Correlation coefficient (ρ) and *P* values between MT model GIC, calculated using both EYR and SWA magnetic fields GIC, and measured GIC for two time intervals during the 07-08 September 2017 storm.

Table 5: Correlation coefficient (ρ) and *P* values between model GIC and observed GIC for the thin-sheet model and the scaled thin-sheet model for three time periods, based on cubic spline interpolation of the observed GIC to a 1-minute sampling interval.

Figure 1.

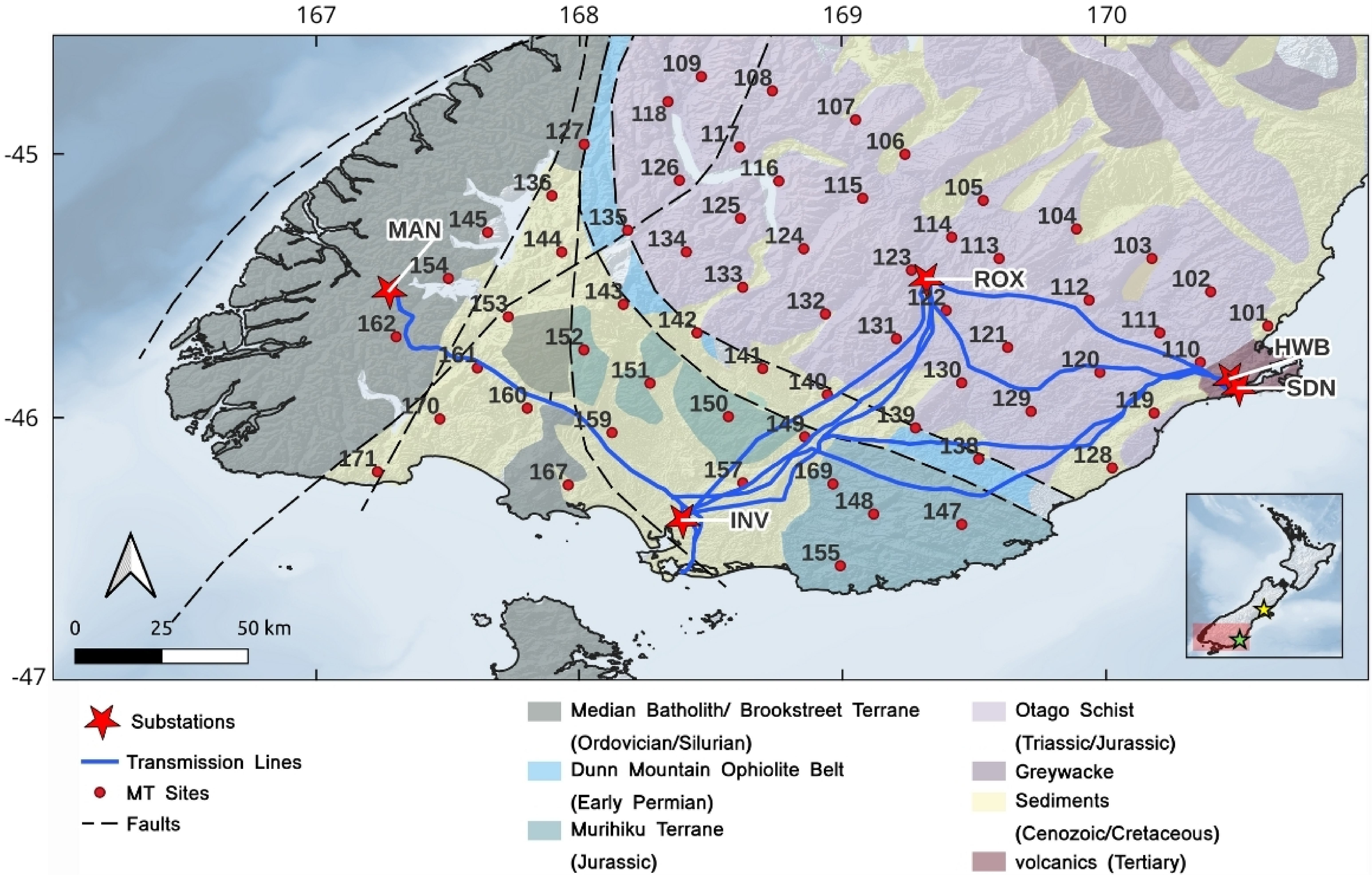
167
168
169
170
-45
-46
-47
MAN
ROX
INV
HWB
SDN
0
25
50 km
Substations
Transmission Lines
MT Sites
Faults
Median Batholith/ Brookstreet Terrane
(Ordovician/Silurian)
Dunn Mountain Ophiolite Belt
(Early Permian)
Murihiku Terrane
(Jurassic)
Otago Schist
(Triassic/Jurassic)
Greywacke
Sediments
(Cenozoic/Cretaceous)
volcanics (Tertiary)

Figure 2.

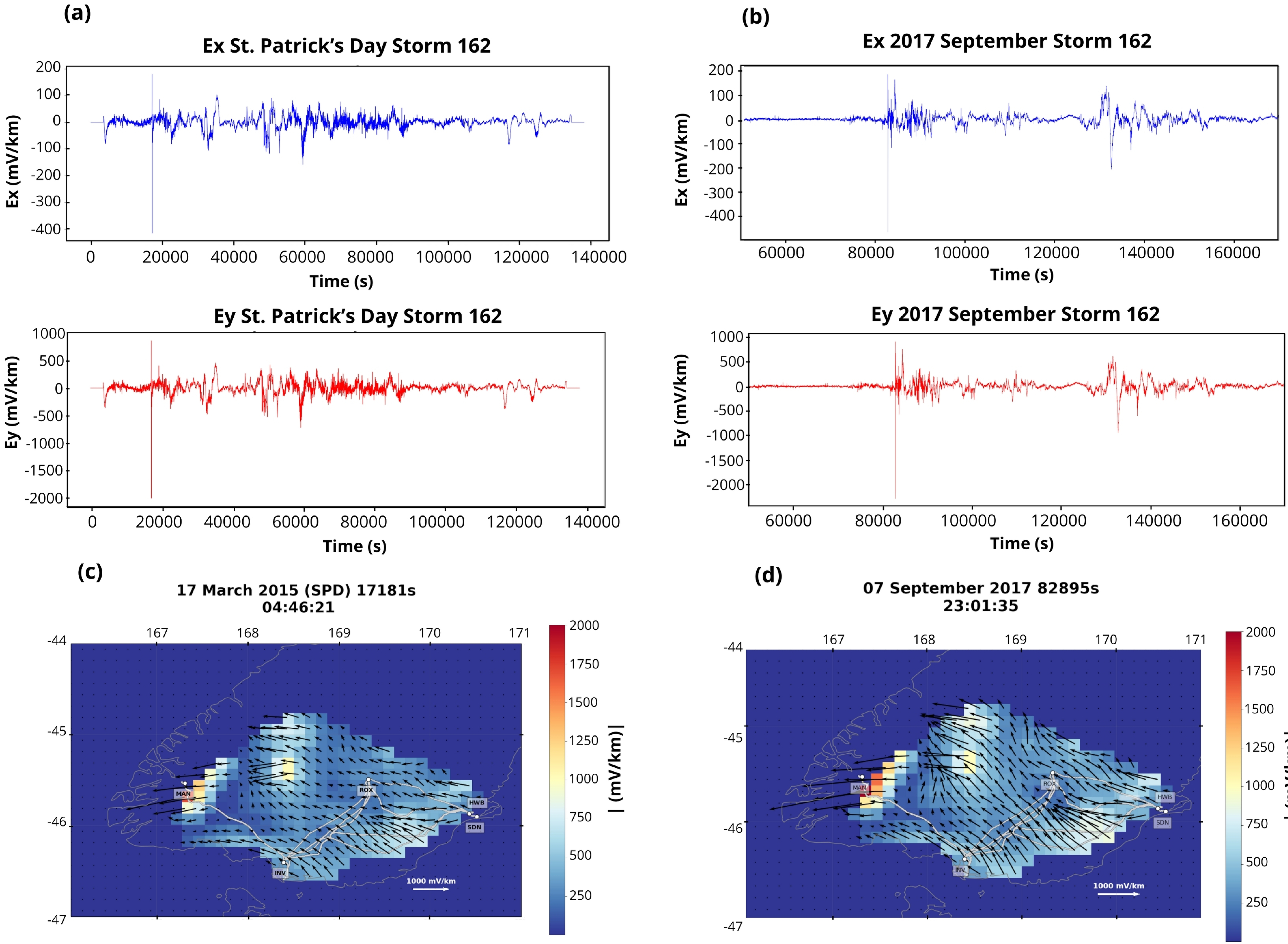

(a)
Ex St. Patrick's Day Storm 162
Ex (mV/km)
Time (s)
Ey St. Patrick's Day Storm 162
Ey (mV/km)
Time (s)
(b)
Ex 2017 September Storm 162
Ex (mV/km)
Time (s)
Ey 2017 September Storm 162
Ey (mV/km)
Time (s)
(c)
17 March 2015 (SPD) 17181s
04:46:21
MAN
ROX
HWB
SDN
INV
1000 mV/km
|E| (mV/km)
(d)
07 September 2017 82895s
23:01:35
MAN
ROX
HWB
SDN
INV
1000 mV/km
|E| (mV/km)

Figure 3.

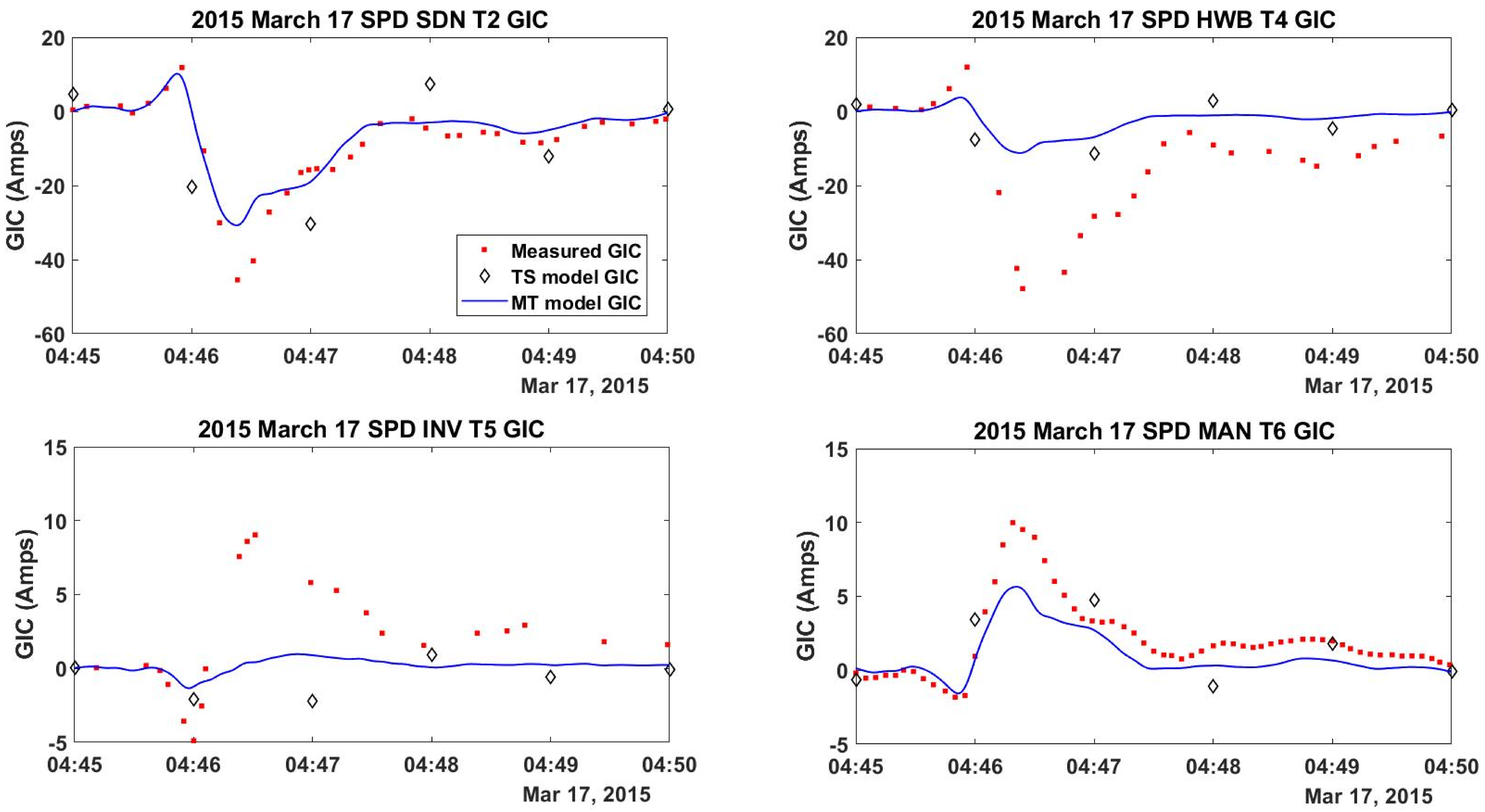

2015 March 17 SPD SDN T2 GIC
GIC (Amps)
20
0
-20
-40
-60
04:45
04:46
04:47
04:48
04:49
04:50
Mar 17, 2015
Measured GIC
TS model GIC
MT model GIC
2015 March 17 SPD HWB T4 GIC
GIC (Amps)
20
0
-20
-40
-60
04:45
04:46
04:47
04:48
04:49
04:50
Mar 17, 2015
2015 March 17 SPD INV T5 GIC
GIC (Amps)
15
10
5
0
-5
04:45
04:46
04:47
04:48
04:49
04:50
Mar 17, 2015
2015 March 17 SPD MAN T6 GIC
GIC (Amps)
15
10
5
0
-5
04:45
04:46
04:47
04:48
04:49
04:50
Mar 17, 2015

Figure 4.

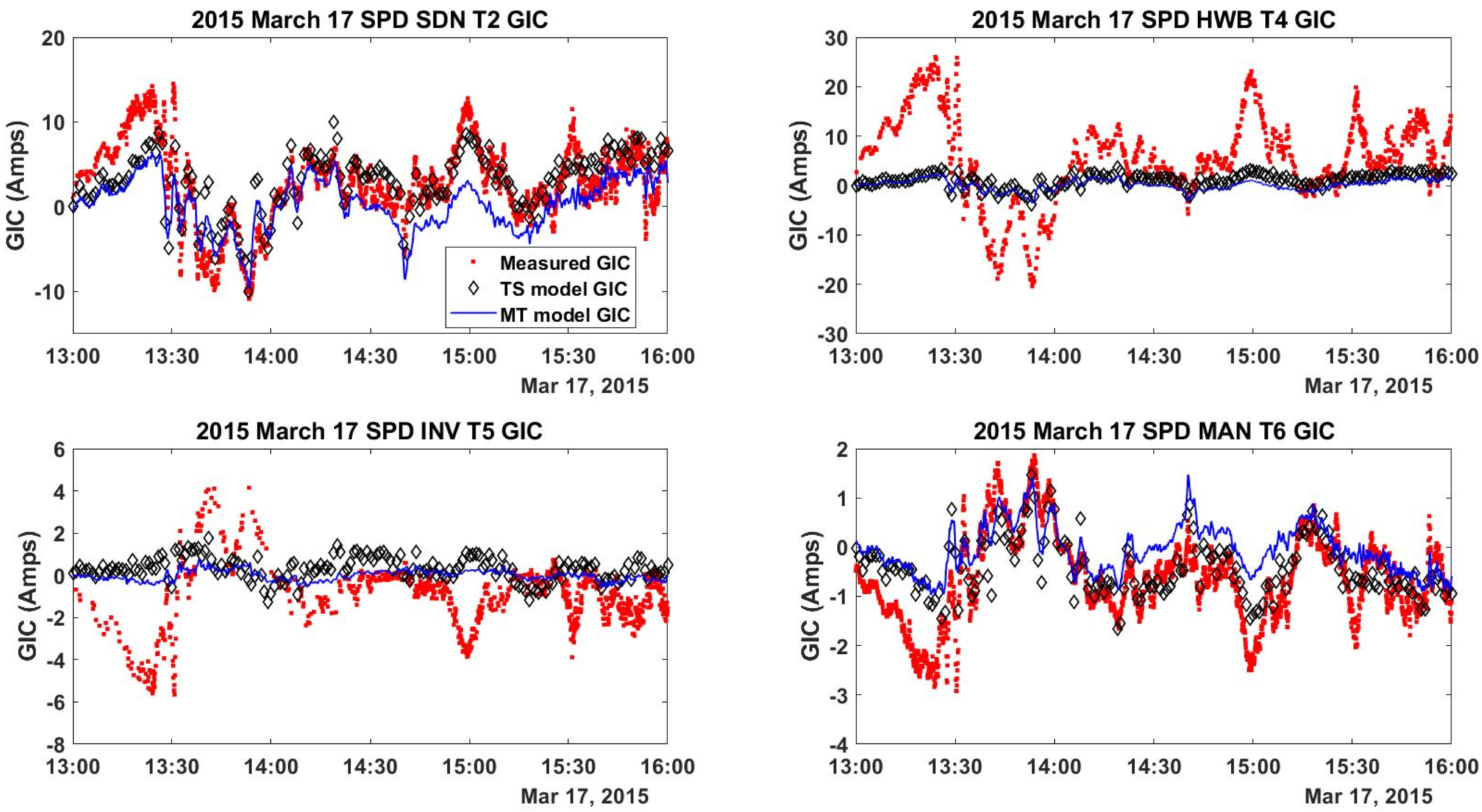
2015 March 17 SPD SDN T2 GIC
GIC (Amps)
Measured GIC
TS model GIC
MT model GIC
20
10
0
-10
13:00
13:30
14:00
14:30
15:00
15:30
16:00
Mar 17, 2015
2015 March 17 SPD HWB T4 GIC
GIC (Amps)
30
20
10
0
-10
-20
-30
13:00
13:30
14:00
14:30
15:00
15:30
16:00
Mar 17, 2015
2015 March 17 SPD INV T5 GIC
GIC (Amps)
6
4
2
0
-2
-4
-6
-8
13:00
13:30
14:00
14:30
15:00
15:30
16:00
Mar 17, 2015
2015 March 17 SPD MAN T6 GIC
GIC (Amps)
2
1
0
-1
-2
-3
-4
13:00
13:30
14:00
14:30
15:00
15:30
16:00
Mar 17, 2015

Figure 5.

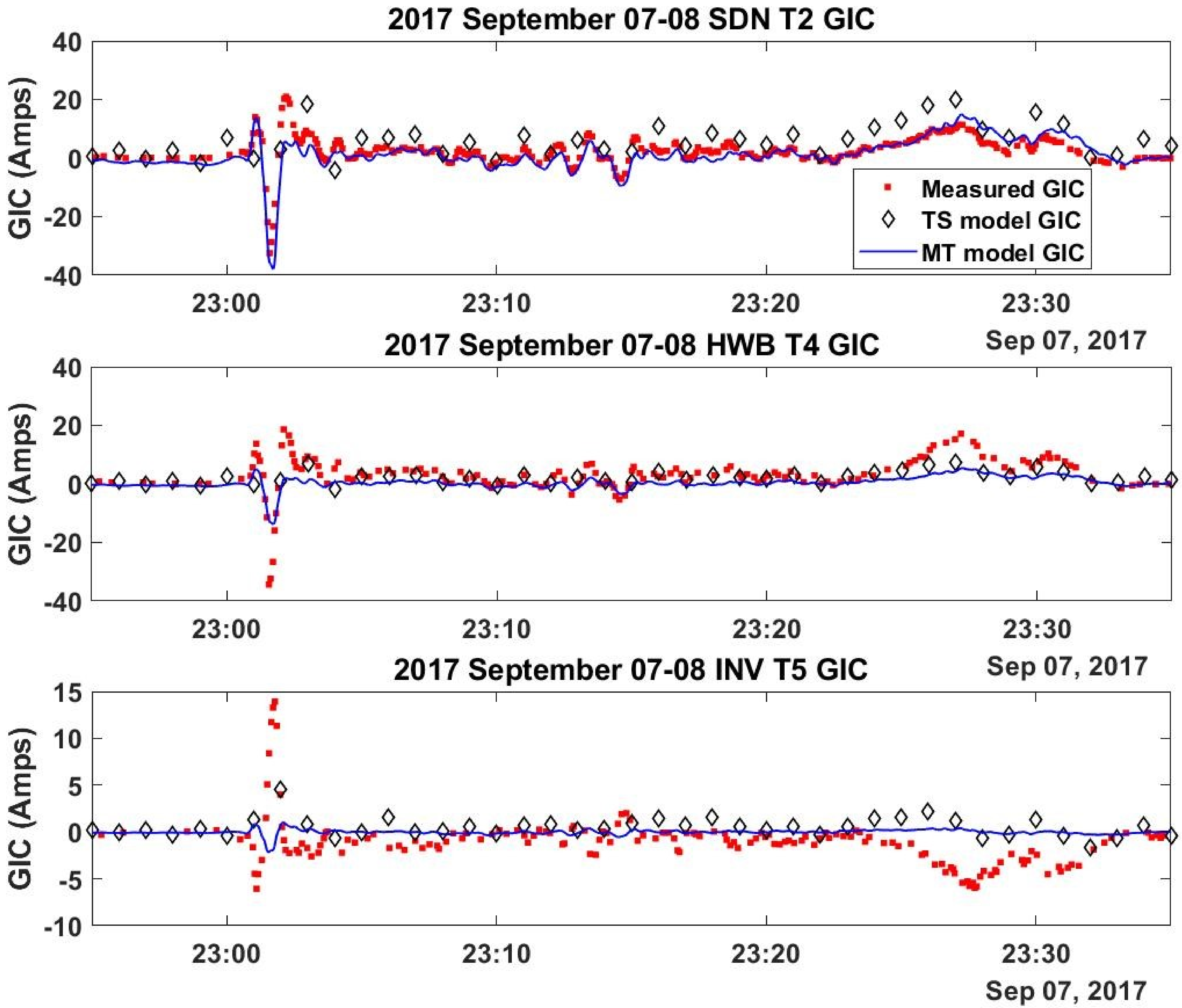
2017 September 07-08 SDN T2 GIC
GIC (Amps)
40
20
0
-20
-40
23:00
23:10
23:20
23:30
Sep 07, 2017
Measured GIC
TS model GIC
MT model GIC
2017 September 07-08 HWB T4 GIC
GIC (Amps)
40
20
0
-20
-40
23:00
23:10
23:20
23:30
Sep 07, 2017
2017 September 07-08 INV T5 GIC
GIC (Amps)
15
10
5
0
-5
-10
23:00
23:10
23:20
23:30
Sep 07, 2017

Figure 6.

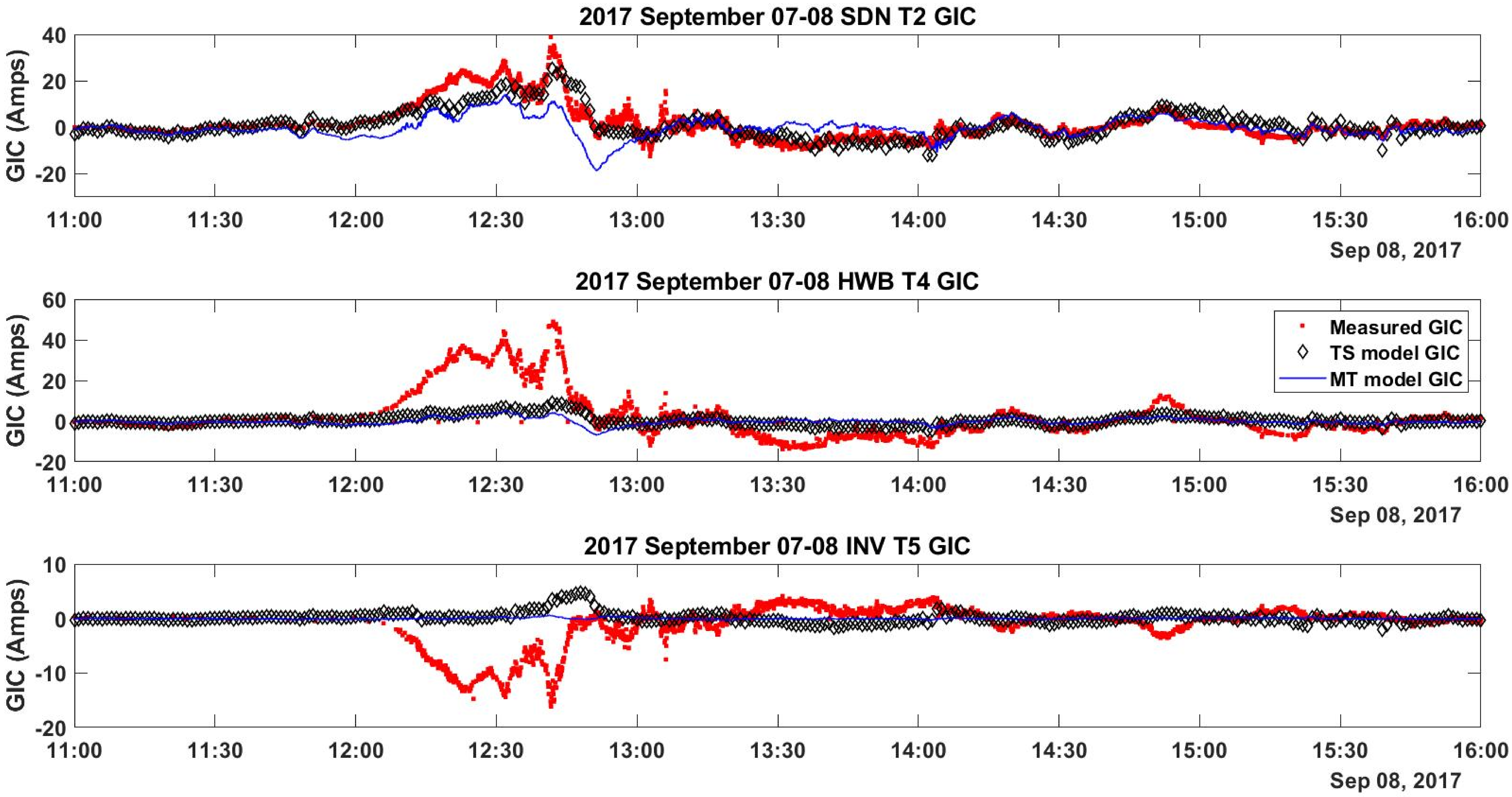

2017 September 07-08 SDN T2 GIC
GIC (Amps)
40
20
0
-20
11:00
11:30
12:00
12:30
13:00
13:30
14:00
14:30
15:00
15:30
16:00
Sep 08, 2017
2017 September 07-08 HWB T4 GIC
GIC (Amps)
60
40
20
0
-20
Measured GIC
TS model GIC
MT model GIC
11:00
11:30
12:00
12:30
13:00
13:30
14:00
14:30
15:00
15:30
16:00
Sep 08, 2017
2017 September 07-08 INV T5 GIC
GIC (Amps)
10
0
-10
-20
11:00
11:30
12:00
12:30
13:00
13:30
14:00
14:30
15:00
15:30
16:00
Sep 08, 2017

Figure 7.

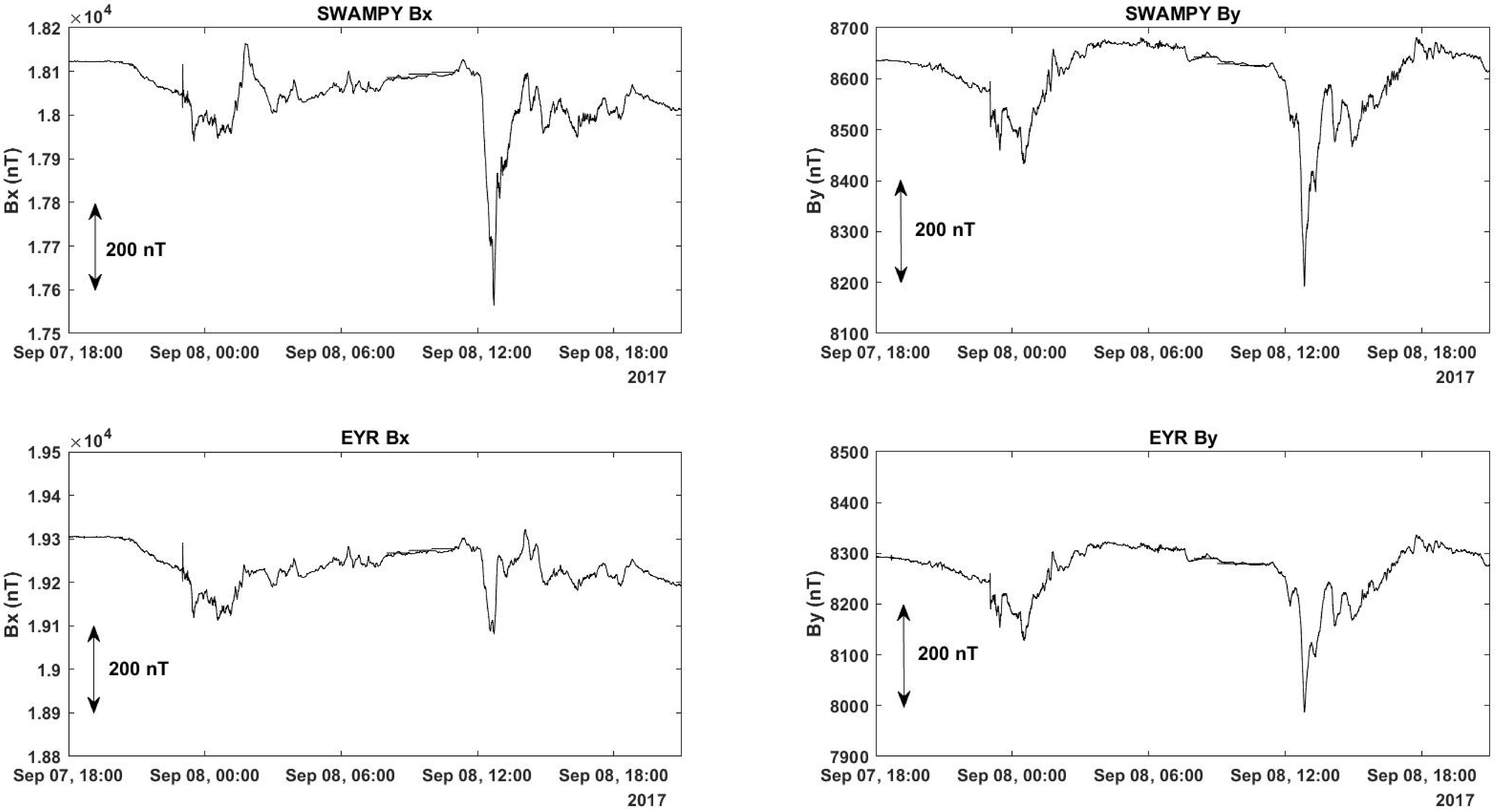
SWAMPY Bx
×10^4
Bx (nT)
200 nT
SWAMPY By
By (nT)
200 nT
EYR Bx
×10^4
Bx (nT)
200 nT
EYR By
By (nT)
200 nT
Sep 07, 18:00
Sep 08, 00:00
Sep 08, 06:00
Sep 08, 12:00
Sep 08, 18:00
2017

Figure 8.

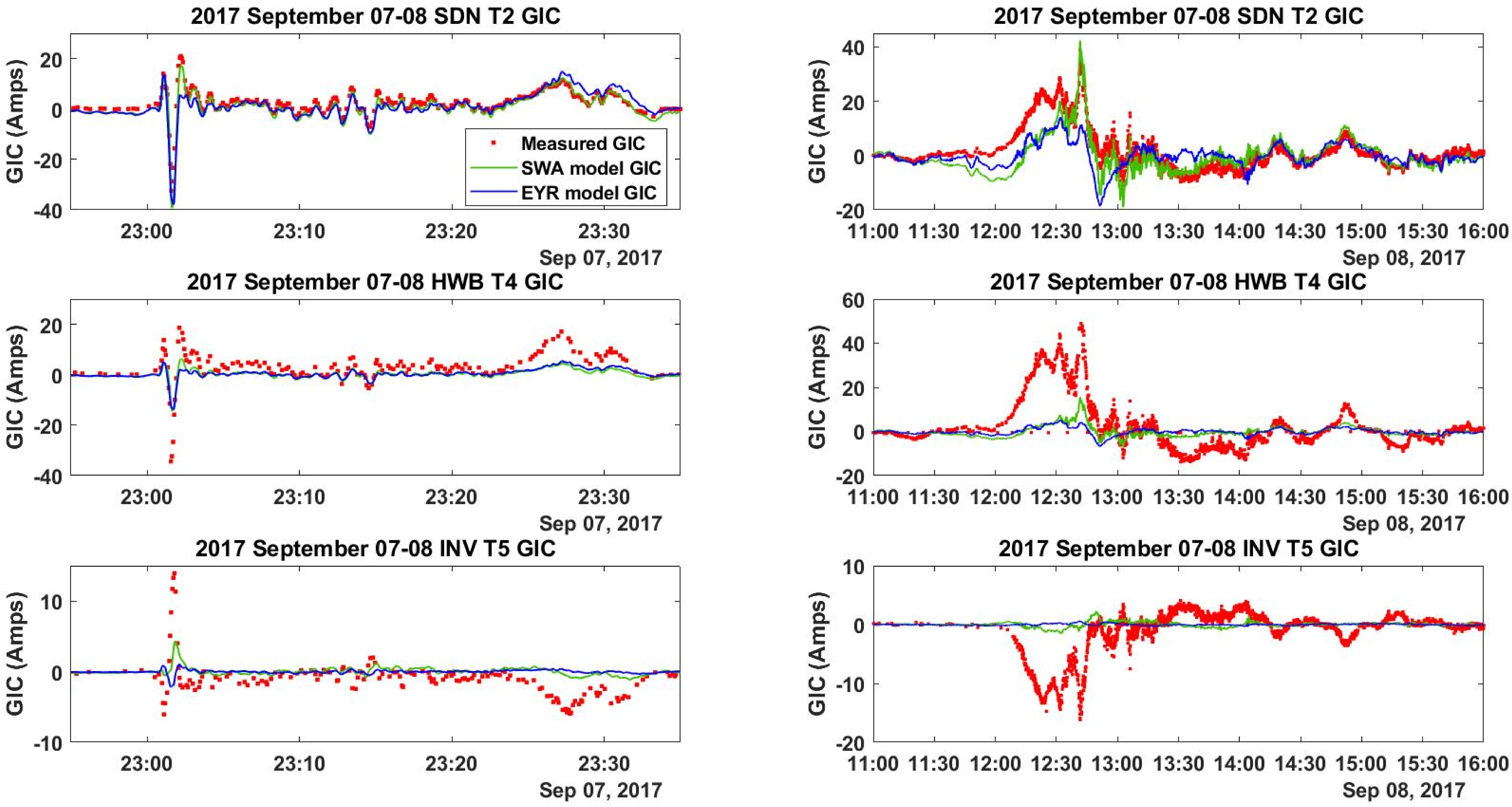

2017 September 07-08 SDN T2 GIC
2017 September 07-08 HWB T4 GIC
2017 September 07-08 INV T5 GIC
GIC (Amps)
Measured GIC
SWA model GIC
EYR model GIC
23:00
23:10
23:20
23:30
Sep 07, 2017
11:00
11:30
12:00
12:30
13:00
13:30
14:00
14:30
15:00
15:30
16:00
Sep 08, 2017

GIC	SDNT2	HWBT4	INVT5	MANT6
Measured	+11.8/-45.5	+11.9/-47.9	-4.9/+9.0	-1.7/+10.0
62 Long Period MT sites	+10.2/-30.7	+3.8/-11.2	-1.3/+1.0	-1.6/+5.7
Thin Sheet Conductance Model (Divett et al., 2020)	-/-30.3	-/-11.3	-2.1/-	-/+4.8
Scaled Thin Sheet Conductance Model (Mac Manus et al., 2022)	-/-12.9	-/-19.3	-3.6/+0.3	-/+2.7

Table 1: Minimum and maximum values (in Amps) of transformer GIC during the SSC of the St. Patrick's Day 2015 Storm.

	SDNT2		HWBT4		INVT5		MANT6	
	ρ	***P***	ρ	***P***	ρ	***P***	ρ	***P***
0445 - 0450 UT (SSC)	0.868	0.506	0.901	0.235	0.494	0.092	0.937	0.526
1300 - 1600 UT	0.745	0.323	0.749	0.091	0.457	0.062	0.743	0.303
0300 - 1800 UT	0.630	0.214	0.644	0.093	0.384	0.055	0.605	0.202

Table 2: Correlation coefficient (ρ) and *P* values between MT model GIC and measured GIC for each transformer considered during 3 intervals of time during the 17 March 2015 storm.

GIC	SDNT2	HWBT4	INVT5
Measured	14.0/-32.5/21.0	13.7/-34.3/18.6	-6.1/13.9/-2.2
62 Long Period MT sites	13.8/-37.9/5.7	5.0/-13.8/2.1	0.9/-2.2/1.1
Thin Sheet Conductance Model (Divett et al., 2020)	- / - /18.4	- / - /6.8	- / - /4.5
Scaled Thin Sheet Conductance Model (Mac Manus et al., 2022)	- / - /13.7	- / - /16.6	- / - /8.0

Table 3: Minimum and maximum values (in Amps) of transformer GIC during the SSC at ~2300 07 September 2017.

	SDNT2		HWBT4		INVT5	
	ρ	***P***	ρ	***P***	ρ	***P***
EYR (2245-2345 07 Sept)	0.739	0.193	0.774	0.280	-0.792	-0.119
SWA (2245-2345 07 Sept)	0.816	0.335	0.784	0.278	0.478	0.102
EYR (1100-1600 08 Sept)	0.587	0.191	0.582	0.076	-0.470	-0.018
SWA (1100-1600 08 Sept)	0.819	0.423	0.801	0.164	0.413	0.047

Table 4: Correlation coefficient (ρ) and *P* values between MT model GIC, calculated using both EYR and SWA magnetic fields GIC, and measured GIC for two time intervals during the 07-08 September 2017 storm.

1300-1600 UT 17 March 2015	**SDNT2**		**HWBT4**		**INVT5**		**MANT6**	
	ρ	***P***	ρ	***P***	ρ	***P***	ρ	***P***
Thin-sheet model	0.747	0.335	0.749	0.361	-0.015	-0.048	0.698	0.285
Thin-sheet scaled	0.797	0.328	0.822	0.113	-0.034	-0.260	0.743	0.300
2245-2345 UT 07 September 2017	**SDNT2**		**HWBT4**		**INVT5**			
	ρ	***P***	ρ	***P***	ρ	***P***		
Thin-sheet model	0.579	-0.331	0.649	0.235	0.200	-0.075		
Thin-sheet scaled	0.604	-0.168	0.686	-0.301	0.124	-0.414		
1100-1600 UT 08 September 2017	**SDNT2**		**HWBT4**		**INVT5**			
	ρ	***P***	ρ	***P***	ρ	***P***		
Thin-sheet model	0.867	0.502	0.871	0.174	-0.345	-0.069		
Thin-sheet scaled	0.871	0.495	0.884	0.503	-0.554	-0.787		

Table 5: Correlation coefficient (ρ) and *P* values between model GIC and observed GIC for the thin-sheet model and the scaled thin-sheet model for three time periods, based on cubic spline interpolation of the observed GIC to a 1-minute sampling interval.